# Concentric Eyewall Formation in Typhoon Sinlaku (2008). Part I: Assimilation of T-PARC Data Based on the Ensemble Kalman Filter (EnKF)

CHUN-CHIEH WU, YI-HSUAN HUANG, AND GUO-YUAN LIEN

*Department of Atmospheric Sciences, National Taiwan University, Taipei, Taiwan*

(Manuscript received 4 March 2011, in final form 11 November 2011)

## ABSTRACT

Typhoon Sinlaku (2008) is a case in point under The Observing System Research and Predictability Experiment (THORPEX) Pacific Asian Regional Campaign (T-PARC) with the most abundant flight observations taken and with great potential to address major scientific issues in T-PARC such as structure change, targeted observations, and extratropical transition. A new method for vortex initialization based on ensemble Kalman filter (EnKF) data assimilation and the Weather Research and Forecasting (WRF) model is adopted in this study. By continuously assimilating storm positions (with an update cycle every 30 min), the mean surface wind structure, and all available measurement data, this study constructs a unique high-spatial/temporal-resolution and model/observation-consistent dataset for Sinlaku during a 4-day period. Simulations of Sinlaku starting at different initial times are further investigated to assess the impact of the data. It is striking that some of the simulations are able to capture Sinlaku's secondary eyewall formation, while others starting the simulation earlier with less data assimilated are not. This dataset provides a unique opportunity to study the dynamical processes of concentric eyewall formation in Sinlaku. In Part I of this work, results from the data assimilation and simulations are presented, including concentric eyewall evolution and the precursors to its formation, while detailed dynamical analyses are conducted in follow-up research.

## 1. Introduction

Concentric eyewalls (CEs) and the eyewall replacement cycle (ERC) in tropical cyclones (TCs) have been widely documented by aircraft observations and high-resolution satellite imagery. Many previous observational studies (e.g., Willoughby et al. 1982; Black and Willoughby 1992; Samsury and Zipser 1995; Willoughby and Black 1996; Hawkins and Helveston 2008; Houze et al. 2006, 2007; Kossin and Sitkowski 2009; Kuo et al. 2009) have depicted the evolution of CE structures. Features easily identified in such a structure include a nearly cloud-free region (moat), and a quasi-circular convection maximum often associated with the horizontal wind maximum outside of the primary eyewall. Statistical analyses based on a 10-yr dataset (1997–2006) showed that on average 70% of the Atlantic, 50% of the eastern Pacific, 40% of the Southern Hemisphere, and 80% of the western Pacific intense storms (>120 kt, where 1 kt = 0.5144 m s$^{-1}$) underwent at least one ERC (Hawkins and Helveston 2008), in which short-term intensity change and expansion of the gale-wind radius can be significant. Coherent statistical results were also obtained in other studies, such as Kossin and Sitkowski (2009) and Kuo et al. (2009). These observational studies have identified CE formation as an important issue in TC forecasting. In addition, numerical simulations have been extensively applied to investigate CE formation in many previous studies (e.g., Willoughby et al. 1984; Nong and Emanuel 2003; Houze et al. 2006, 2007; Kuo et al. 2004; Terwey and Montgomery 2008; Wang 2009; Qiu et al. 2010). From dynamical analyses and sensitivity experiments among those observational and numerical studies, a number of factors or mechanisms have been suggested as contributors to CE formation. Nevertheless, forecasting and simulating the formation of CE remain a challenging issue. To better understand and forecast CE formation, it is critical to clarify key mechanisms and factors for secondary eyewall formation (SEF).

Several studies have indicated that the topography influences eyewall structure and perhaps helps the formation of the secondary eyewall (e.g., Hawkins 1983; Wu et al. 2003, 2009). A series of papers (Willoughby 1979;

---

*Corresponding author address:* Chun-Chieh Wu, Department of Atmospheric Sciences, National Taiwan University, No. 1, Sec. 4, Roosevelt Rd., Taipei 106, Taiwan.
E-mail: cwu@typhoon.as.ntu.edu.tw

DOI: 10.1175/MWR-D-11-00057.1

Willoughby et al. 1982, 1984) have shown that several processes are likely to play important roles in CE formation, including asymmetric friction due to the storm's motion, updrafts triggered by nearby downdrafts associated with the moat, and ice microphysics. Recently, Terwey and Montgomery (2008) pointed out that the topographic effect, the asymmetric friction due to TC motion and model-ice microphysics are not essential for CE formation based on their numerical simulations, although these factors can have impacts on the evolution of the CE structure and cycle. For instance, in contrast to the control experiment in Terwey and Montgomery (2008), the secondary eyewall formed a couple of hours earlier along with a more intensive outer eyewall in their no-ice experiment. More recently, Zhou and Wang (2011) studied the impacts of ice-phase microphysics on the evolution of ERC, including its formation time, duration, radii of eyewalls, and the associated intensity change. They also found that the adopted microphysics scheme can have considerable influence on the intensity change and evolution of the CEs. Other observations and numerical simulations (e.g., Nong and Emanuel 2003; Ortt and Chen 2006, 2008; Hill and Lackmann 2009; Wang 2009) suggested that external forcing relevant to high environment humidity can influence storm size, rainband structure, and hence may also provide an ambient condition favorable for CE formation. Nong and Emanuel (2003) indicated that sustained eddy angular momentum fluxes arising from interactions between a mature TC and its environment could develop secondary eyewall features, which may invigorate the wind-induced surface heat exchange (WISHE; Yano and Emanuel 1991) and thus contribute to the establishment of a secondary eyewall. Wang (2009) and Hill and Lackmann (2009) showed that high ambient humidity can enhance latent heat release in the vortex outer-core region, which may further provide a favorable environment for expansion of storm size, rainband(s) formation/intensification, and even CE formation.

Meanwhile, internal forcing has also been investigated and has been suggested to play a role during CE formation from various aspects in the literature. It has been proposed that the accumulation of energy near the stagnation or critical radii of vortex Rossby waves (VRWs; e.g., Montgomery and Kallenbach 1997; Brunet and Montgomery 2002; Montgomery and Brunet 2002) can have impacts on the outer rainband structure and perhaps on CE formation (e.g., Chen and Yau 2001; Chen et al. 2003; Wang 2002a,b; Corbosiero et al. 2006; Qiu et al. 2010; Abarca and Corbosiero 2011; Martinez et al. 2011). Houze et al. (2007) found that simulation of ERC failed when the model resolution decreased from 1.67 to 5 km. Meanwhile, they noticed that during the ERC in Rita, the small-scale features captured by the radar in the inner-core region, may be related to the VRW dynamics. Accordingly, they suggested the importance of high model resolution to better simulate small-scale internals of a TC vortex, and the importance of targeting the small-scale structures in a TC by aircraft surveillance.

The role of the axisymmetrization process has also been shown to be important. For instance, extending from studies on fundamental vortex dynamics (Melander et al. 1987; McWilliams 1990; Dritschel and Waugh 1992; Fuentes 2004) and based on the barotropic nondivergent model, Kuo et al. (2004) suggested that the primary vortex can axisymmetrize weak potential vorticity (PV) patches into the secondary vortex ring, provided that the primary vortex is strong enough compared to the outer disturbances. However, recent studies (e.g., Terwey and Montgomery 2008; Moon et al. 2010) noted that PV patches outside the eyewall can be of comparable magnitude to that in the eyewall region both in the real TC environment and in their simulations with more realistic physical processes included (such as the moist convection). In particular, Moon et al. (2010) indicated that the interaction between the TC core vortex and the convection-induced small vorticity dipoles of considerable strength in two-dimensional flows does not lead to the formation of a coherent concentric vorticity ring. Thus, the axisymmetrization process under a simplified two-dimensional incompressible flow appears incomplete for describing SEF in the real atmosphere. The role of the three-dimensional moist process in the maintenance of a vorticity ring has also been indicated in the study of eyewall evolution by Wu et al. (2009).

Terwey and Montgomery (2008) presented a new moist-based $\beta$-skirt axisymmetrization (BSA) formation hypothesis as an intrinsic CE formation mechanism. This hypothesis requires a region with long filamentation time (Rozoff et al. 2006) and a sufficient low-level radial PV gradient ($\beta$) associated with the primary swirling flow, moist convective potential, and the follow-up WISHE process. Meanwhile, Wang (2008) indicated that inner rainbands are present in regions with filamentation time shorter than 30 min, suggesting that the filamentation process has an entirely different role from that in Rozoff et al. (2006). Instead of suppressing the convection, the filamentation effect is argued to cause the axisymmetrization of vorticity in the rapid filamentation zone.

As introduced in this section, some studies found that intrinsic mechanisms are important, while others suggested that external forcing and environmental conditions are crucial. Moreover, with previous works mostly based on limited observations or numerical simulations with idealized settings, it is still not well understood what the key mechanisms or conditions are for CE formation in the real atmosphere. The CE cycles in a real TC are neither fully documented by observation nor well simulated by numerical models. One of the major difficulties is insufficient spatial and temporal coverage of TC observations, especially the coverage of data over the inner-core region, which is important for validation and for construction of the initial vortex in a model. Another major roadblock is the insufficient understanding of the physical processes in the evolution of TCs, which are critical in constructing adequate model physics for numerical simulations. These concerns reveal that the integration of good data, a capable numerical model, an efficient data assimilated methodology, and an effective vortex initialization scheme are indispensable for thorough investigation of the dynamics of CE formation and for improvement of the model forecast in a real case.

In 2008, an international field experiment, The Observing System Research and Predictability Experiment (THORPEX) Pacific Asian Regional Campaign (T-PARC; Elsberry and Harr 2008) was conducted, providing an opportunity to investigate extensive TC research issues such as genesis, structure change, targeted observation, and extratropical transition. Typhoon Sinlaku (2008), a case in point under T-PARC, has the most abundant flight observations conducted and possesses great potential in addressing major scientific issues in T-PARC, such as targeted observation (Chou et al. 2011; Harnisch and Weissmann 2010; Weissmann et al. 2011; Wu et al. 2011, manuscript submitted to *Mon. Wea. Rev.*). Meanwhile, a new TC vortex initialization method based on the ensemble Kalman filter (EnKF; Wu et al. 2010), which effectively provides well-balanced initial TC vortex structure dynamically consistent with the model, is employed in this study. By continuously assimilating (with an update cycle every 30 min) all available data, including conventional soundings, 159 dropwindsondes and Stepped Frequency Microwave Radiometer (SFMR) data from 9 T-PARC flight missions during Sinlaku from 9 to 13 September, this study constructs a unique high-spatial/temporal-resolution and model/observation-consistent dataset for Sinlaku. This dataset provides a unique opportunity to investigate key mechanisms and conditions of CE formation in Sinlaku.

Following our study, a series of papers will be presented to show results of our investigation in the intensity and structure evolution in Sinlaku during the CE cycle based on model results from data assimilations and simulations. This paper (Part I) presents general features of the assimilations and simulations. Detailed dynamical analyses and physical examinations for the CE process are discussed in follow-up papers [e.g., axisymmetric dynamical processes; Huang et al. (2012, hereafter Part II)]. In the following section (section 2), methodology and data will be introduced. The results will be presented in section 3, including the track, intensity, and structure evolution in Sinlaku, particularly during the CE cycle. The CE structure and evolution are shown with various diagrams (time–radius diagrams, vertical cross sections, horizontal structure, etc.) using different parameters, including wind fields, (potential) vorticity, and total column rain rate, etc. Conclusions and issues to be further investigated are provided in section 4.

## 2. Methodology and data

### *a. A new vortex initialization method based on EnKF along with additional data*

The ensemble Kalman filter, first proposed by Evensen (1994), has been shown to have potential applications in data assimilations of weather systems, including TCs, in a number of studies (Snyder and Zhang 2003; Zhang et al. 2004, 2006, 2009; Chen and Snyder 2007; Zhang and Snyder 2007; Fujita et al. 2008; Meng and Zhang 2007, 2008a,b; Torn and Hakim 2009; Yussouf and Stensrud 2010). Following previous works using EnKF for TC forecasts (e.g., Chen and Snyder 2007; Torn and Hakim 2009; Zhang et al. 2009), Wu et al. (2010) developed a new vortex initialization method on a WRF-based EnKF data assimilation system (Meng and Zhang 2008a,b). Three special observational parameters of TCs (TC center position, the storm motion vector, and the axisymmetric surface wind profile) are adopted and assimilated via the EnKF methodology. The TC center position and storm motion vector are mainly estimated from satellite imagery and are available from major operational centers. The axisymmetric surface wind profile can be constructed with an empirical formula from Willoughby et al. (2006) based on any kind of observation products available, such as satellite imagery, conventional radiosondes and buoys data, and in situ measurement from aircraft observations, etc. Amid these, data obtained from aircraft surveillance provide particularly valuable information on the TC structure and intensity, especially when the TC is over an open-ocean area. Analyses of the case of Typhoon Fung-wong (2008) in Wu et al. (2010) demonstrated that this new method can effectively make use of the three key TC parameters previously mentioned to establish a dynamically balanced vortex structure for follow-up TC simulations.

With the two key items in place [i.e., the TC initialization method from Wu et al. (2010) and plentiful data for Sinlaku during T-PARC], this paper provides a means to assimilate detailed T-PARC data based on the continuous EnKF update cycles to reconstruct the trajectory and evolution of Sinlaku, and thus offers an

TABLE 1. T-PARC data assimilated into simulations of Typhoon Sinlaku (2008).

| | | Dropwindsondes | | | | |
|---|---|---|---|---|---|---|
| | | | | | USAF C-130 | |
| | Conventional radiosondes | DOTSTAR Astra | DLR Falcon | NRL P-3 | Inner core | Others |
| Sounding amount | 623 | 36<br>(2 flights) | 34<br>(2 flights) | 12<br>(1 flight) | 20<br>(4 flights) | 57 |
| | | 159 | | | | |

opportunity to investigate the CE structure and physical processes of SEF. Benefitting from the efficiency of the EnKF method, fast update cycle ensemble simulations can be conducted without expensive computation costs. Available data on Sinlaku (Table 1 and Fig. 1), including 623 conventional radiosondes from the Global Telecommunication System (GTS), 159 dropwindsondes and SFMR data from 9 T-PARC flight missions [e.g., the Dropwindsonde Observations for Typhoon Surveillance near the Taiwan Region (DOTSTAR; Wu et al. 2005, 2007) Astra jet, the German Aerospace Center (DLR) Falcon, and the Naval Research Laboratory (NRL) P-3; see Elsberry and Harr (2008)] are integrated and assimilated into the model every 30 min with 28 ensemble members for each experiment. As shown in Fig. 1, locations of the adopted data are marked by symbols shaded with different colors for different observations or flight missions. Information on the structure of Sinlaku is shown in Fig. 2, including wind profiles observed by C-130's reconnaissance flights, dropwindsonde data from DOTSTAR, and the radii of 34-, 50-, and 64-kt wind and maximum wind analyzed at the Joint Typhoon Warning Center (JTWC). Spiral rainbands with significant convective activities are found outside the eyewall prior to SEF (Fig. 2d), while no coherent secondary wind maximum is found (Fig. 2c). The double-eyewall structure of Sinlaku is documented by the two wind maxima in the C-130 mission at 1207 and 1331 UTC 11 September (Fig. 2e) and by satellite images from 0445 to 2132 UTC 11 September (e.g., Fig. 2f). After this period, C-130 data and satellite images show the dissipation of the inner eyewall and the appearance of an ERC (Figs. 2g,h).

These abundant data of Sinlaku during T-PARC clearly help define the axisymmetric surface wind structure, which is one of the three TC parameters for the new vortex initialization method in Wu et al. (2010). In this study, Sinlaku's center position and motion vector are obtained based on the best track from the Japan Meteorological Agency (JMA). The axisymmetric surface wind profiles assimilated into the simulations (thick line in the left panel of Fig. 2) are mainly based on the SFMR surface wind data from four C-130 eyewall-penetrating reconnaissance missions (the $\alpha$-pattern flight path shown in the right panel of Fig. 2), along with the 10-m surface winds estimated by dropwindsonde data from two DOTSTAR targeted surveillance observation missions (path shown with black lines in Figs. 2d,f).

### b. *Model settings and experimental design*

The Advanced Research Weather Research and Forecasting (ARW-WRF) model (version 2.2.1) is employed to perform update cycle ensemble simulations. The horizontal grid spacing is 45 km (81 × 76 grid points), 15 km (88 × 100 grid points), and 5 km (82 × 82 grid points) for the first (D1), second (D2), and third (D3 or D3′) domains, respectively (Fig. 3). The third domain is a moveable nest with two-way feedback, centered at the vortex center to ensure that the TC

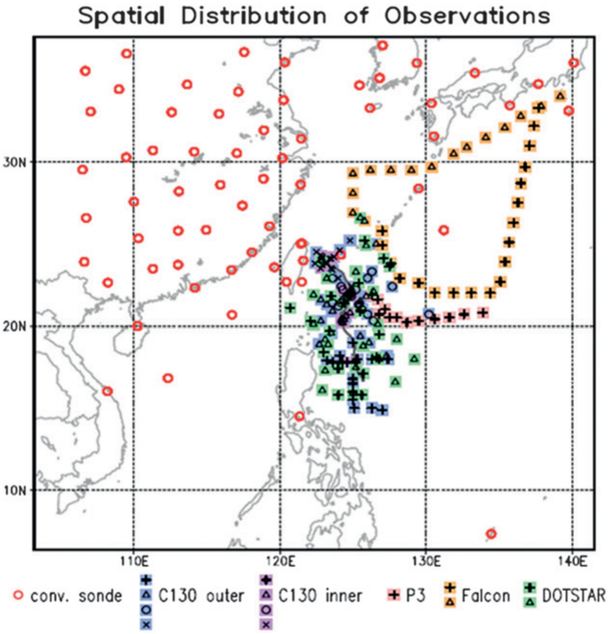

FIG. 1. Observation data assimilated into the model. Conventional radiosondes are denoted by red circles, and dropwindsondes deployed from the four aircrafts during T-PARC are denoted by other symbols shaded in different colors.

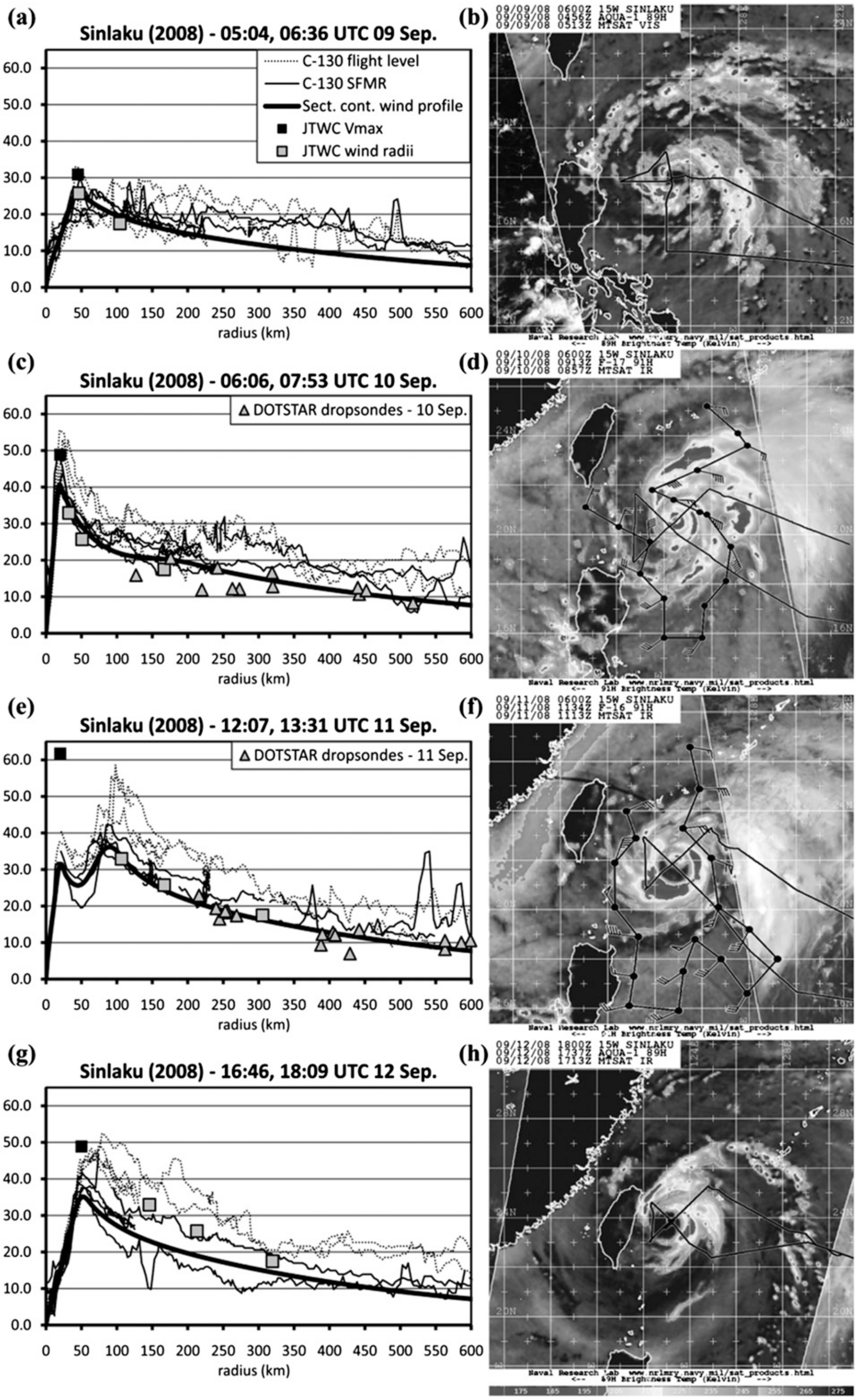

FIG. 2. (a),(c),(e),(g) The tangential wind profiles assimilated into the model (thick lines) constructed mainly based on data from C-130 (gray lines for the flight level wind and black lines for SFMR surface wind) along with combined information from JTWC (RMW: black squares; wind radii of 34, 50, and 64 kts: gray squares) and the available DOTSTAR dropwindsonde data (triangles). (b),(d),(f),(h) Polar-orbiting satellite images from 85-GHz sensors, superposed with the flight path (the $\alpha$ pattern is C-130, and the other is DOTSTAR) and deployed locations of the DOTSTAR dropwindsondes (black dots).

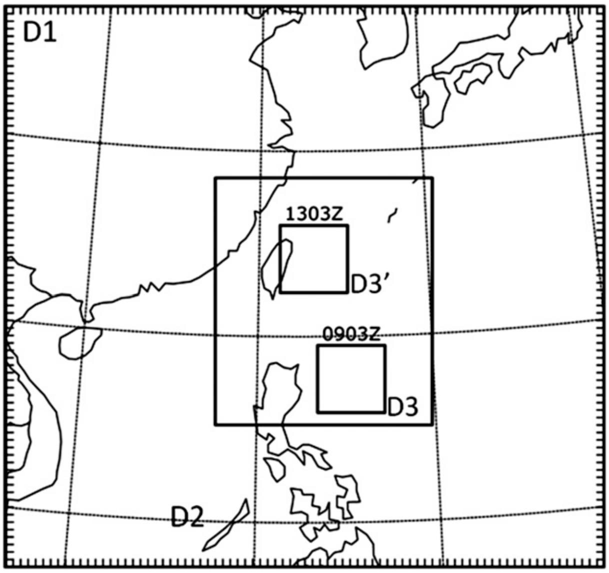

FIG. 3. Model domains: D1, D2, and D3 (D3′). D3 (D3′) is a moving nest that is activated from 0300 UTC 9 Sep (D3) to the end of the simulation (0300 UTC 13 Sep; D3′).

inner-core region is resolved by the finest grid. The two-way vortex-following nest technique is implemented in both forward model simulations and the EnKF update. The model is run with 35 vertical levels in the terrain-following sigma coordinate (as in Wu et al. 2010). The final analysis (FNL, 1° × 1°) taken from the National Centers for Environment Prediction (NCEP) and the optimally interpolated microwave SST (OISST) are utilized for the initial and boundary conditions.

The adopted parameterization schemes are the same as those in the simulations of Fung-wong in Wu et al. (2010). The WRF Single-Moment 6-Class Microphysics scheme (WSM6; Hong et al. 2004; Hong and Lim 2006) is used in the simulations. Other parameterization schemes adopted in the model are the Rapid Radiative Transfer Model (RRTM) scheme (Mlawer et al. 1997) for longwave radiation, the simple shortwave scheme (Dudhia 1989) for shortwave radiation, and the Yonsei University (YSU) planetary boundary layer scheme (Hong et al. 2006). The cumulus convection is parameterized with the Grell–Dévényi ensemble scheme (Grell and Dévényi 2002) only in the coarser domains, namely, D1 and D2 (Fig. 3). The NCEP Final Analysis (FNL) at 1200 UTC 8 September 2008 is taken as the initial ensemble mean to construct the 28 ensemble members [see section 2b in Wu et al. (2010), for the methodology used while creating the initial perturbations]. After the prerun in the first 5 h, the cycling assimilation run is carried out from 1700 UTC 8 September to 0300 UTC 13 September. To reduce computation costs, the vortex-following nest is initiated at 0300 UTC 9 September before the additional aircraft data are included. The overall assimilation period is more than 4 days, covering Sinlaku's lifetime, from formation to development, intensification, and the CE cycle.

The ensemble simulations with all data assimilated throughout the integration are regarded as the control experiment (CTL), which contains 28 ensemble members updated and integrated independently during a typical EnKF cycle. In this paper, most figures showing the results of a single storm are derived from the ensemble mean (the average of the 28 ensemble members; hereafter CTL_m). The CE cycle in CTL_m is investigated in detail in section 3. To assess the impact of cumulative data in different amounts, forecasting experiments are performed with assimilation paused at different times. Several ensemble forecasts, EXP1103, EXP1015, and EXP1003, are conducted with initial conditions taken from CTL at 0300 UTC 11 September, 1500 UTC 10 September, and 0300 UTC 10 September, respectively (Table 2). The results (mostly with the ensemble mean) are discussed in section 3e.

## 3. Results

### a. *Track and minimum sea level pressure for all ensemble members and the ensemble mean (CTL_m)*

As introduced in the previous section, conventional data and three special parameters of TCs are assimilated into the model throughout the integration in CTL. Figure 4a shows tracks of the 28 ensemble members and their ensemble mean (CTL_m) superposed on the best track from the JMA, indicating that all ensemble members closely follow the best track of Sinlaku

TABLE 2. Experimental design: CTL and the forecasting experiments.

| Expt | Assimilation of new data | SEF time (defined in terms of $\bar{v}$ at the lowest model level in their ensemble mean) |
|---|---|---|
| CTL | Throughout the integration | 0700 UTC 11 Sep |
| EXP1103 | Terminated after 0300 UTC 11 Sep | 0700 UTC 11 Sep |
| EXP1015 | Terminated after 1500 UTC 10 Sep | 0730 UTC 11 Sep |
| EXP1003 | Terminated after 0300 UTC 10 Sep | No SEF |

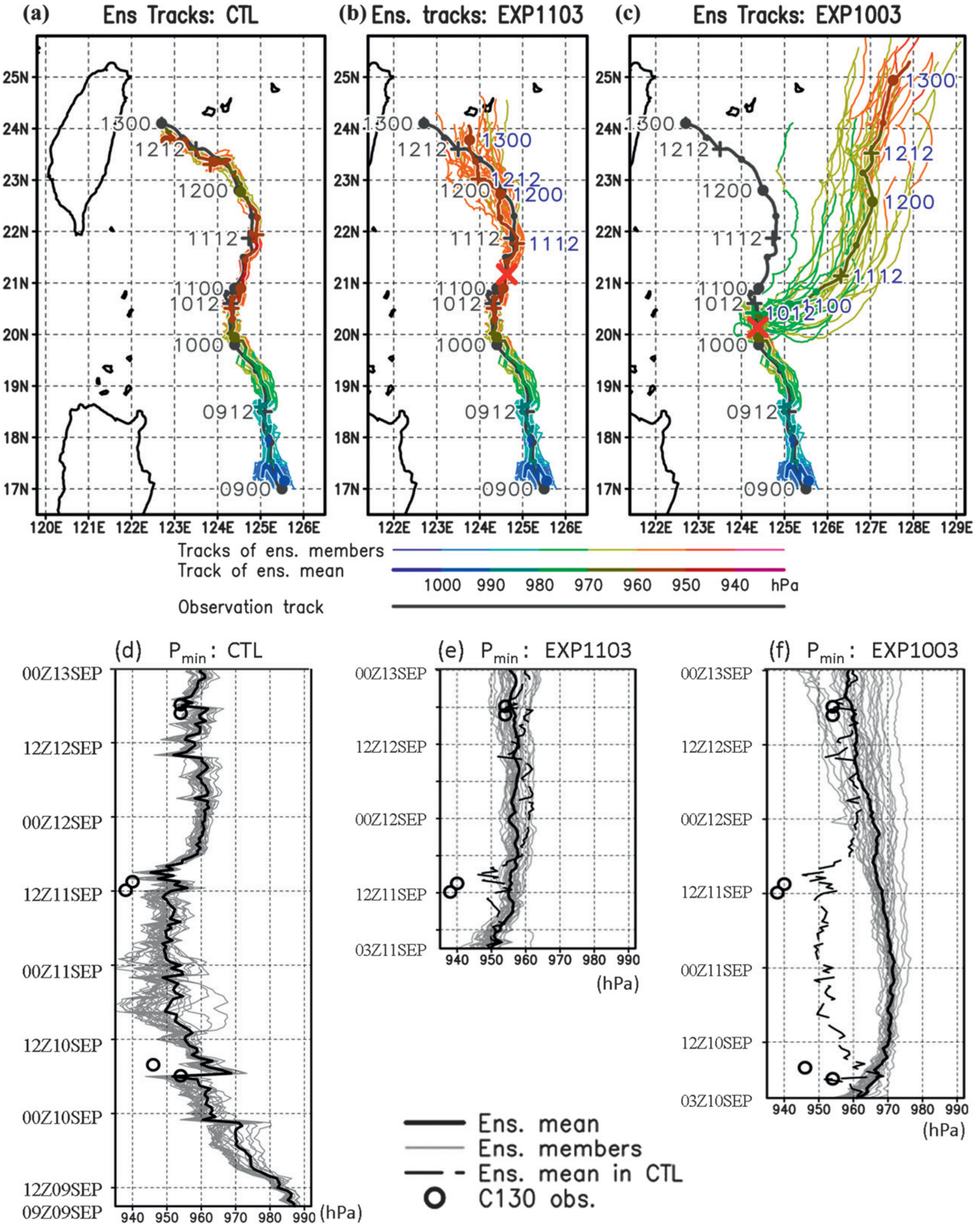

FIG. 4. Simulated tracks in (a) CTL, (b) EXP1103, and (c) EXP1003. The best track obtained from JMA is in black. The thick color line refers the ensemble mean in each experiment. Thin lines indicate each ensemble member, while the colors represent different levels of intensity (see the color bar). The crisscross mark in (b) and (c) indicates the initial time of the forecast experiment. (d)–(f) The corresponding minimum sea level pressure to each experiment. Black and gray lines are for the results in the ensemble mean and ensemble members, respectively. The black circles represent the minimum sea level pressure from the C-130 observation.

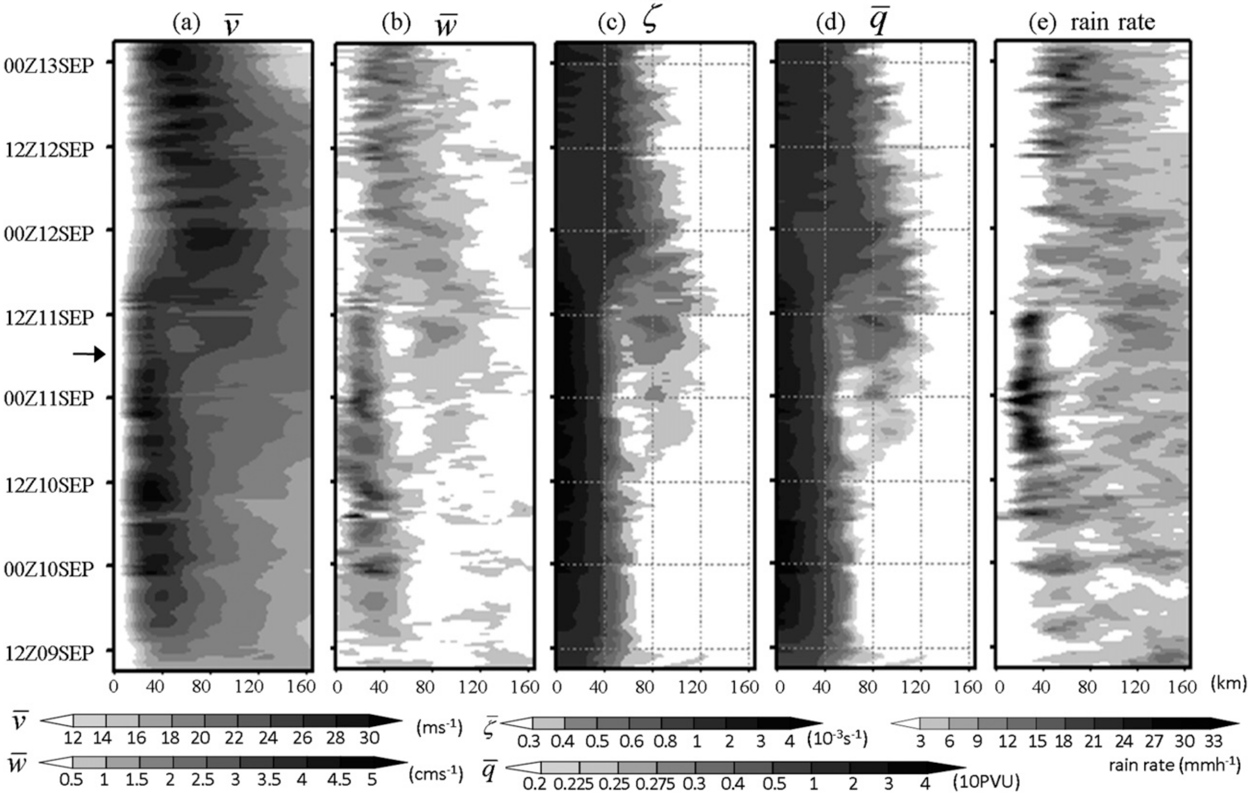

FIG. 5. For CTL, time–radius diagrams of the azimuthally mean (a) tangential wind (m s$^{-1}$) at the lowest model level, (b) vertical velocity (m s$^{-1}$) at 0.5-km height, (c) relative vorticity (10$^{-3}$ s$^{-1}$) at 2-km height, (d) potential vorticity (10 PVU) at 2-km height, and (e) the total column rain rate (mm h$^{-1}$) in the ensemble mean (average of 28 ensemble members, also denoted by CTL_m). SEF time is indicated by an arrow on the *y* axis.

throughout the integration with a limited ensemble spread. Moreover, evolution of the minimum sea level pressure is also well simulated (Fig. 4d) (except at around 0800 UTC 10 September, when the minimum sea level pressure is oversimulated) as compared with the independent measurement from C-130 reconnaissance flights (black circles in Fig. 4d), which is not used for data assimilation. The result indicates that the central sea level pressure of Sinlaku in CTL continuously deepens before around 1700 UTC 10 September, the time when the axisymmetric upward motion (its ensemble mean is shown in Fig. 5b) in the outer region begins to strengthen. Afterward, the storm intensity remains stable for 19 h. At the time when an ERC is completed (at 1800 UTC 11 September, as discussed in section 3b), the central sea level pressure rises significantly from 945 to 960 hPa in 3 h. With the capability to capture the evolution of Sinlaku's track and intensity, these ensemble runs from CTL are further analyzed as shown below.

### *b. Azimuthally mean structure of CTL_m*

First, we investigate the overall axisymmetric structure of CTL_m. Major azimuthal mean variables, including tangential wind $\overline{v}$, radial velocity $\overline{u}$, vertical velocity $\overline{w}$, relative vorticity $\overline{\zeta}$, potential vorticity $\overline{q}$, and total column rain rate, are shown both in time–radius diagrams (Fig. 5) and in vertical cross sections (Fig. 6). Information in time–radius diagrams is shown at the lowest model level (about 10-m height) for $\overline{v}$, at an altitude of 0.5 km for $\overline{w}$ (for the purpose of investigating the friction-induced upward motion within the boundary layer, which is relevant to Part II) and 2 km for $\overline{\zeta}$ and $\overline{q}$. The CE cycle is particularly worth noting in these figures. All the azimuthally mean parameters in Fig. 5 well demonstrate the secondary eyewall structure in Sinlaku, with differences in the formation time between secondary maximums using different parameters. The SEF time in this paper is defined by $\overline{v}$ at the lowest model level ($\eta = 0.998\,85$). By examining the $\overline{v}$ profile (such as those in the left panel of Fig. 2) at different times (figures not shown), we can precisely recognize the SEF (the persistent secondary maximum) and define its formation time in each simulation. For instance, the SEF time is 0700 UTC 11 September in CTL_m. Based on the time–radius diagram of $\overline{v}$, the outer (secondary) eyewall is initially present at the radii of about 80–120 km from the

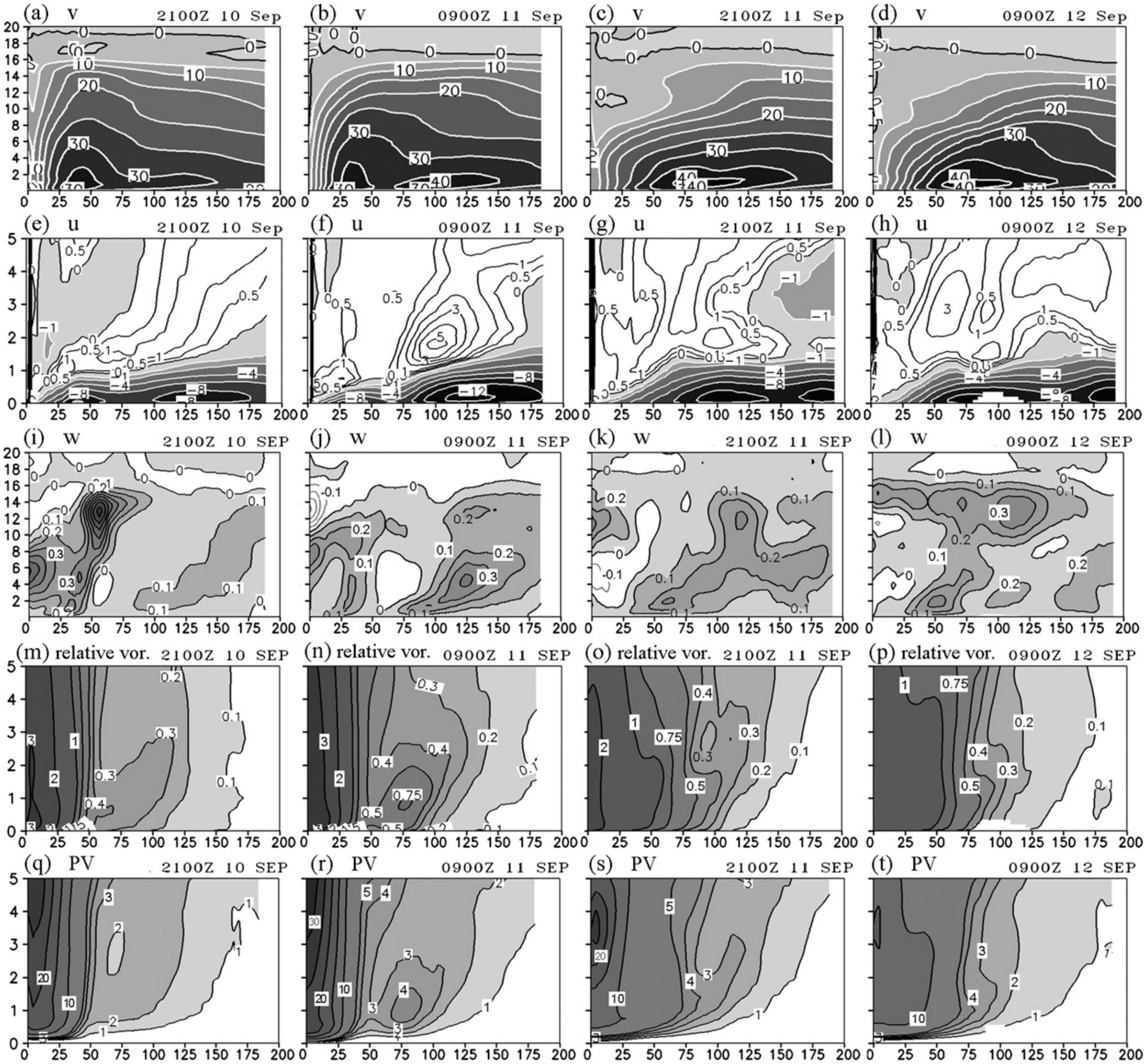

FIG. 6. The radius–height cross sections of the azimuthally averaged variables in CTL_m. (a)–(d) Tangential winds, contour interval is 5 m $s^{-1}$, and cyclonic winds are shaded. (e)–(h) Radial winds, inflow is shaded with a 2 m $s^{-1}$ contour interval, and the contour interval for outflow is 1 m $s^{-1}$. (i)–(l) Vertical velocity, contour interval is 0.1 m $s^{-1}$, and upward motion is shaded. (m)–(p) Relative vorticity, contour interval is $10^{-3}$ $s^{-1}$ when it is larger than $1 \times 10^{-3}$ $s^{-1}$, and is $1 \times 10^{-4}$ $s^{-1}$ when it is smaller than $0.5 \times 10^{-3}$ $s^{-1}$. Values of $0.5 \times 10^{-3}$ and $0.75 \times 10^{-3}$ $s^{-1}$ are additionally plotted, and values larger than $0.1 \times 10^{-3}$ $s^{-1}$ are shaded. (q)–(t) Potential vorticity, contour interval is 5 PVU when it is larger than 5 PVU, and 1 PVU when it is smaller than 5 PVU. Values larger than 1 PVU are shaded.

storm center (Fig. 5a). During the CE process, from 0700 to 1800 UTC 11 September, both inner and outer eyewalls experience sporadic intensification and weakening. During later stages of the CE cycle (between 1200 and 1800 UTC 11 September), competition between the inner and outer eyewalls is observed. Finally, the outer eyewall replaces the disintegrated inner eyewall and becomes the new primary eyewall at 1800 UTC 11 September, and thus an ERC is completed. As to the evolution of the azimuthally mean vertical velocity $\overline{w}$ and total column rain rate, it can be found that convective activities outside the primary eyewall intensify significantly around 0700 UTC 11 September (Figs. 5b,e), indicating the enhancement of organized convection outside the inner eyewall. A moat region where convection is suppressed is also found between the two eyewalls during the same period. Convection associated with the inner eyewall decays after about 1400 UTC 11 September. Eventually, the inner eyewall is replaced by the new outer convection while Sinlaku becomes a storm with a larger eye. These features of the CE cycle are consistent with those on $\overline{v}$. However, the secondary maxima of $\overline{w}$ and the total column rain rate appear much earlier than that of $\overline{v}$. In section 3c, the plan view demonstrates those weak secondary maxima of convective activities featuring spiral rainbands, rather than a CE structure. Other variables, such as $\overline{\zeta}$ (Fig. 5c) and $\overline{q}$ (Fig. 5d), also indicate the presence of SEF in Sinlaku. Both $\overline{\zeta}$ and $\overline{q}$ at 2-km height show a coherent secondary maximum, which increases significantly around the SEF time, showing the CE structure.

With regard to the evolution of the storm's vertical structure, the azimuthal average of radius–height cross sections for CTL_m is also investigated (Fig. 6). After the spinup process (figures not shown), vertical structures in terms of $\overline{v}$, $\overline{u}$, $\overline{\zeta}$, and $\overline{q}$ show a unique observation/model consistence with the CE evolution processes. The radius of the maximum tangential wind (RMTW) near the surface is located around 30 km from the storm center before SEF (Fig. 6a), indicating a compact vortex structure. The double-eyewall structure is clearly shown at lower levels (approximately below 5 km) in terms of $\overline{v}$, with the radii of the inner and outer eyewalls at about 35 and 100 km (Fig. 6b), respectively. After ERC, the new eyewall is located at around 100 km from the typhoon center (Fig. 6c), showing a big-eye structure in Sinlaku. Then the vortex intensifies and the new eyewall contracts with time. The $\overline{v}$ maximum near the surface in Fig. 6d, for example, is about 45 m $s^{-1}$ and is located at the radius of 60 km from the storm center. This reintensification and contraction are also present in Fig. 5a.

The secondary maximum of the radial inflow is first shown at 2100 UTC 10 September (Fig. 6e), but the magnitude is weaker than that in the eyewall. It is worth noting that the intensification of boundary layer inflow occurs over the region where the secondary eyewall forms and establishes prior to SEF. After SEF, inflow over the outer eyewall becomes much larger than that in the inner eyewall (Fig. 6f). The maximum inflow in the inner eyewall weakens and eventually disappears (Figs. 6g,h), demonstrating the completion of an ERC. As for $\overline{w}$, the eyewall features a slantwise convection from the surface to about 16-km altitude, associated with a broad but weak upward motion region outside the radius of 75 km prior to SEF (e.g., Fig. 6i). After SEF, convection in the inner eyewall becomes shallower and much weaker, while an upward motion substantially develops in the outer eyewall (e.g., Fig. 6j). After ERC, the outer convection becomes a new primary eyewall located at a larger distance from the storm center. Then, convection in the new eyewall moves radially inward and strengthens with time. The structure and intensity evolution in terms of $\overline{v}$, $\overline{u}$, and $\overline{w}$ are consistent with those in a typical CE cycle.

Furthermore, the vertical structure on $\overline{\zeta}$ and $\overline{q}$ shows a similar evolution during the CE cycle (Figs. 6m–p,q–t). Both $\overline{\zeta}$ and $\overline{q}$ decrease with radius. The $\overline{\zeta}$ and $\overline{q}$ gradients are larger within the eye and eyewall region ($r < 50$ km in Figs. 6m,q), while being smoother outside the eyewall region. A local maximum appears just inside the radius of the secondary maximum $\overline{v}$ in both the $\overline{\zeta}$ and $\overline{q}$ fields during the CE episode, and is confined to levels below 2.5 km (Figs. 6n,r). After the ERC (Figs. 6o,s), the gradient over the eye and inner eyewall region decreases significantly, and the low-level maximum over the outer eyewall vanishes. However, a local maximum appears in the midlevel from around 2.5 to 5 km. During the eyewall contraction period, the magnitude of $\overline{\zeta}$ and $\overline{q}$ in the eye continue decreasing, and their gradients over the eye region become very small, demonstrating a nearly homogeneous structure in $\overline{\zeta}$ and $\overline{q}$ (Figs. 6p,t). In all, the axisymmetric structure of CTL_m demonstrates the double-eyewall structure and the CE cycle in terms of various variables, including $\overline{v}$, $\overline{w}$, $\overline{\zeta}$, and $\overline{q}$, and the total column rain rate (Figs. 5 and 6).

Regarding the SEF issue, what we are concerned about are the features prior to SEF. One of the interesting features is that the secondary maxima of $\overline{w}$ (Fig. 5b), $\overline{\zeta}$ (Fig. 5c), and $\overline{q}$ (Fig. 5d) initially appeared around 1800 UTC 10 September, which is about 13 h earlier than the SEF time defined by a persistent secondary maximum of $\overline{v}$. About 6 h before the secondary maxima of $\overline{\zeta}$ and $\overline{q}$ are established, the weak secondary maxima of $\overline{\zeta}$ and $\overline{q}$ are found to move outward radially from the inner eyewall between 1200 and 1800 UTC 10 September. Meanwhile, the outer tangential wind field ($\overline{v}$; Fig. 5a) keeps broadening since about 1200 UTC 10 September, corresponding to the outward shift of these outer maxima prior to SEF. The broadening of the outer tangential wind is mostly confined to the lower levels (Fig. 6a), while radial inflow in the boundary layer considerably strengthens over the same region (Fig. 6e). These features occurring prior to SEF are speculated to serve as key precursors to SEF. Detailed dynamical analyses (such as the energy collection of VRWs, the upscale process of the eddy kinetic energy on the $\beta$-skirt, boundary layer dynamics, and the role of the environmental moisture, etc.) are to be presented in Part II and Part III of this study.

While the azimuthally mean structure highlights general features of a CE structure, to provide a more detailed eyewall structure, plan views are also examined in section 3c.

### c. *Plan views of CTL_m*

The plan views of each dynamical variable investigated in section 3b, such as $v$, $w$, $\zeta$, $q$, and the total column rain rate, are examined at a 30-min time interval. The evolution of Sinlaku's structure in CTL_m in different fields is shown by 2-h plots from 1800 UTC 10 September to 0000 UTC 12 September (Figs. 7–11). In the $v$ field, the storm is intense, compact (small eye), and quite symmetric at 1800 UTC 10 September (Fig. 7a). The tangential wind field broadens over the northwestern and southeastern quadrants between 1800 UTC 10 September and 0000 UTC 11 September (Figs. 7a–d), consistent with the broadening wind field previously identified from the axisymmetric view (Figs. 5a and 6a). The secondary maximum of the swirling circulation becomes more organized and develops along with time in the northwestern quadrant (Figs. 7e,f) while the primary eyewall becomes relatively weaker. Afterward, the outer circulation gradually surrounds the primary eyewall and nearly completely encloses it from 0600 to 1200 UTC 11 September (Figs. 7g–j), demonstrating a typical CE structure. Between 1200 and 1800 UTC 11 September, some disturbances show up near the secondary eyewall, and the CE structure becomes less distinct (Figs. 7j–l). This transition period of eyewall evolution, which is also shown in $w$, $\zeta$, and $q$ fields (see Figs. 8, 10, and 11), corresponds to the sudden weakening of the secondary eyewall near 1200 UTC 11 September in Fig. 5. During the development of the outer swirling circulation (Figs. 7e–g) and the CE period (Figs. 7g–l), the original primary eyewall (inner eyewall) weakens and the eye enlarges slightly. After 1800 UTC 11 September, the inner eyewall dissipates (Fig. 7m), and the overall vortex intensity weakens. The outer eyewall replaces the original one and becomes the new primary eyewall with a bigger eye (Figs. 7m–p).

Similar evolution can be found in $w$ and the total column rain-rate fields (Figs. 8 and 9). Convection cells form sporadically in rainbands outside of the eyewall. Not well organized to begin with (Figs. 8a–e and 9a–e), they eventually dissipate or merge into the eyewall. However, after 0400 UTC 10 September, these rainbands become more organized outside and along the (inner) eyewall (Figs. 8f,g and 9f,g). The intense but sporadic convective activities in spiral rainbands project a weak maximum onto the azimuthal-mean structure prior to SEF (Figs. 5b,e). This implies that the secondary maximum in the azimuthal mean of convective activities is not a robust index for identifying a CE structure. Eventually, the rainbands coalesce to form an annular convection ring outside the inner eyewall (Figs. 8h–j and 9h–j). As in $v$ field, the distribution of $w$ also becomes disturbed and the CE structure is less distinct between 1200 and 1800 UTC 11 September (Figs. 8j–l). After this short-term adjustment, deep convective rings over the inner and outer eyewall regions are again recognizable (Fig. 8l). Convection in the inner eyewall gradually collapses (Figs. 8m–o), and the secondary eyewall becomes the new primary eyewall (Fig. 8p). In contrast, the rain-rate distribution is much less disturbed between 1200 and 1600 UTC 11 September (Figs. 9j–l). The less disturbed mass fields (e.g., temperature and water contents; figures not shown) can be part of the reasoning. Besides, it is also important to keep in mind the fact that the total column rain rate reflects the integrated column property composed of multiple variables. The rain-rate field may thus appear smoother. The heavy precipitation region over the inner eyewall quickly dries out and turns into a nonprecipitation area (Figs. 9k,l) when the CE structure becomes less distinct. After that, an annular precipitating region forms along with the establishment of a new primary eyewall (Figs. 9l–p).

The $\zeta$ and $q$ fields have very similar patterns in the simulation (Figs. 10 and 11). Before the eyewall replacement, the vorticity (and PV) field has a monopole structure with a prominent radially negative gradient and with its maximum at the center. Small-scale vorticity or PV patches grow and decay sporadically outside the eyewall before 2300 UTC 10 September (figures not shown). However, at a point between 2000 and 2200 UTC 10 September (Figs. 10b,c and 11b,c), these vorticity patches become considerably organized into a beltlike structure (Figs. 10d–g and 11d–g). Being wrapped up, they form a vorticity ring outside the primary core from 0800 to 1000 UTC 11 September (Figs. 10h–i and 11h–i). Similar to the wind field, the ring structure in the $\zeta$ and $q$ fields outside the parent vortex becomes less distinct and contains high-wavenumber disturbances between 1200 and 1600 UTC 11 September (Figs. 10j–l and 11j–l). Then, the ring structure in $\zeta$ and $q$ dissipates, and a monopole with a smaller radial gradient is found (Figs. 10m–p and 11m–p), indicating the completion of an ERC. Particularly important is that the precursory small vorticity eddies outside the primary vorticity core before SEF are of comparable magnitude to those over the primary eyewall. These vorticity patches are about 3 times weaker than the average vorticity over the core vortex (e.g., $r < 50$ km in Figs. 6m,q; 10c–f; and 11c–f). For instance, as to PV at 2 km, the patches range from 3 to 10 potential vorticity units (PVU; 1 PVU = $10^{-6}$ K m$^2$ kg$^{-1}$ s$^{-1}$) (Figs. 11c–f), while those near the eyewall range from 5 to 15 PVU (Figs. 6q and 11c–f) and the averaged value in the core vortex is about 15 PVU. As suggested in Moon et al. (2010), these characteristics of the vorticity wrap-up process cannot be demonstrated by an axisymmetrization process in the framework of two-dimensional dry barotropic dynamics (e.g., Kuo et al. 2004) and require an interpretation based on a more sophisticated model with a three-dimensional dynamical core.

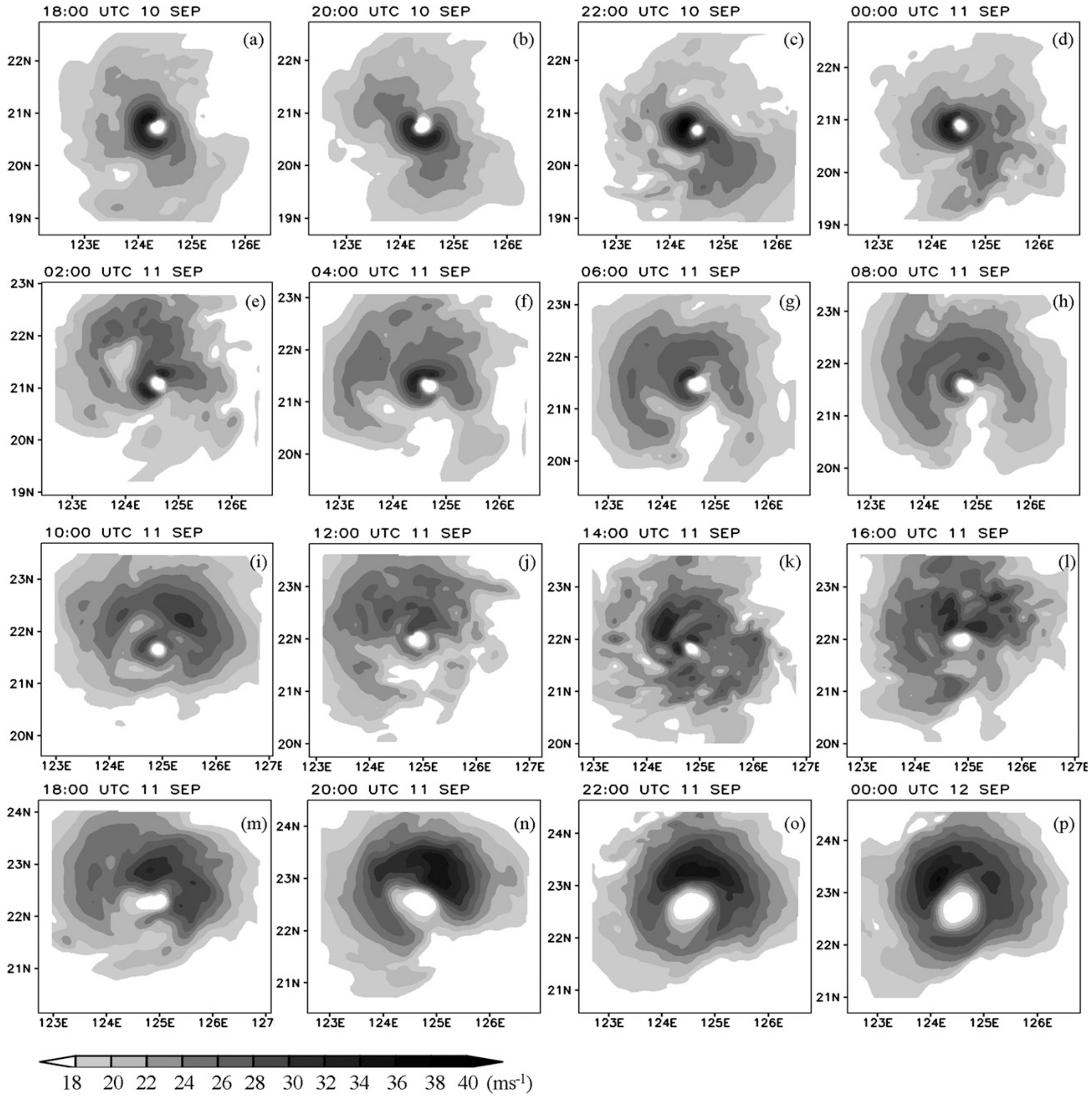

FIG. 7. Plan view of the tangential winds (m s$^{-1}$) at the lowest model level in CTL_m from 1800 UTC 10 Sep to 0000 UTC 12 Sep with 2-h time intervals.

### *d. The CE cycle in each ensemble member*

The time series plots of the RMTW at the lowest model level in all the 28 ensemble members of CTL are displayed in Fig. 12, showing that vortices in each member undergo a CE cycle. The ensemble spread of RMTW shows a ±10-km deviation from the ensemble mean. Despite the small differences in SEF time, the duration of the CE cycle, and the radii of the eyewalls from the vortex center, all ensemble members in the control experiment are able to capture the CE cycle of Sinlaku.

### *e. Sensitivity to the amount of assimilated data*

To evaluate the impact of data, ensemble forecasts of Sinlaku are carried out at different initial times. EXP1103, EXP1015, and EXP1003 stand for ensemble simulations initialized at 0300 UTC 11 September,

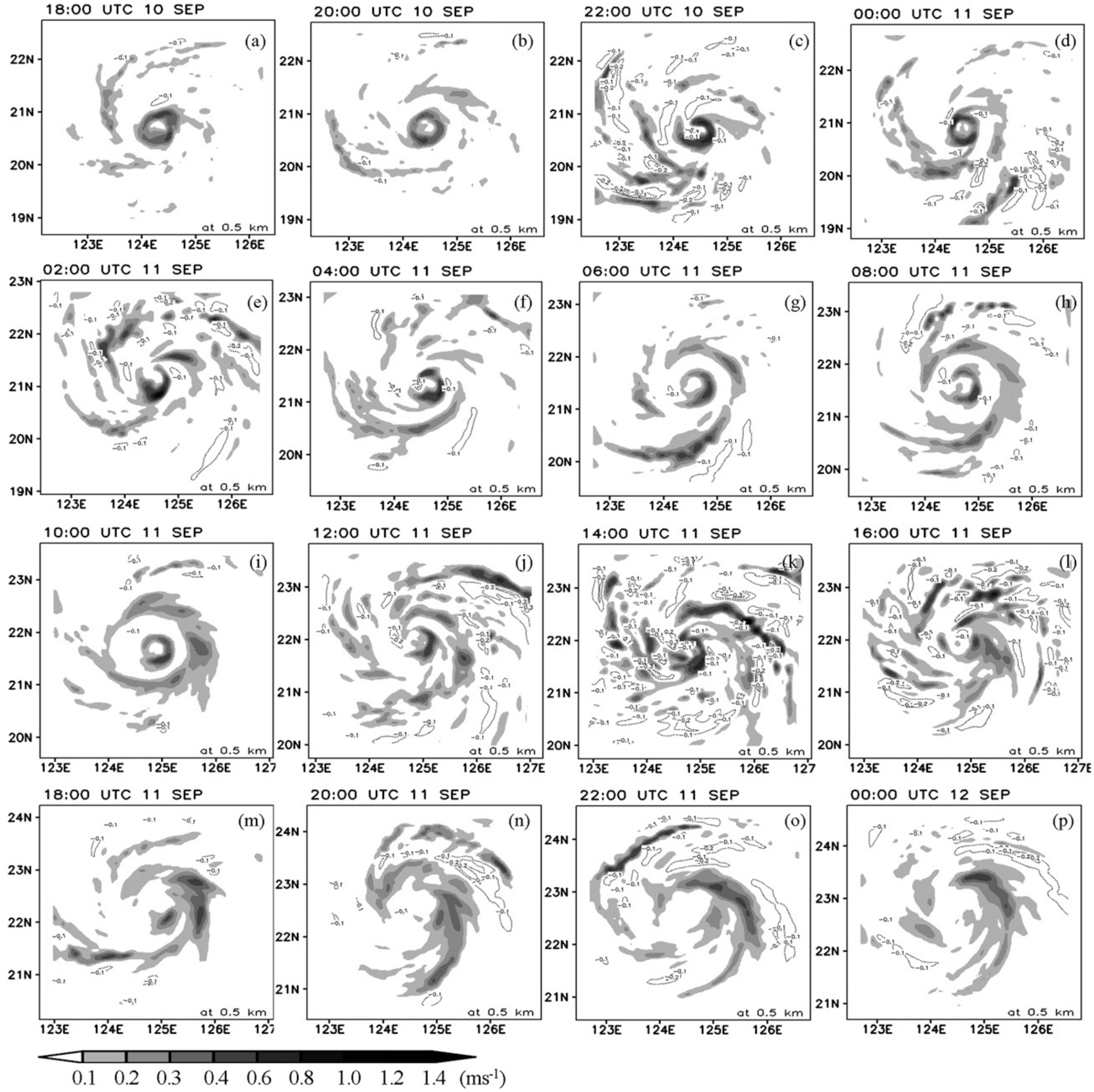

FIG. 8. As in Fig. 7, but for the vertical velocity (m $s^{-1}$) at 0.5-km height. Upward motion is shaded with gray colors, while descent motion is marked by contours.

1500 UTC 10 September, and 0300 UTC 10 September, respectively (Table 2). Note that the ensemble means of these experiments (i.e., EXP1103_m, EXP1015_m, and EXP1003_m) without data assimilation are not averaged from the corresponding ensemble members at each time because TC tracks tend to spread out quickly (Figs. 4b,c) and, therefore, the averaged fields cannot well represent the overall TC intensity and structure. Instead, the ensemble means denote corresponding simulations initialized in CTL_m.

The time–radius diagrams of $\overline{v}$, $\overline{w}$, $\overline{\zeta}$, $\overline{q}$, and the total column rain rate demonstrate that a CE structure is present in EXP1103_m (Fig. 13) and EXP1015_m (Fig. 14), while the CE feature in EXP1015_m is not as robust as that in EXP1103_m. Tracks (Fig. 4b) and intensity (Figs. 4e and 13a) in EXP1103 are well simulated, although missing the sharp deepening of the central sea level pressure prior to SEF (Fig. 4e). The SEF time for EXP1103_m is 0700 UTC 11 September, the same as that in CTL_m. SEF in EXP1015_m occurs 30 min later

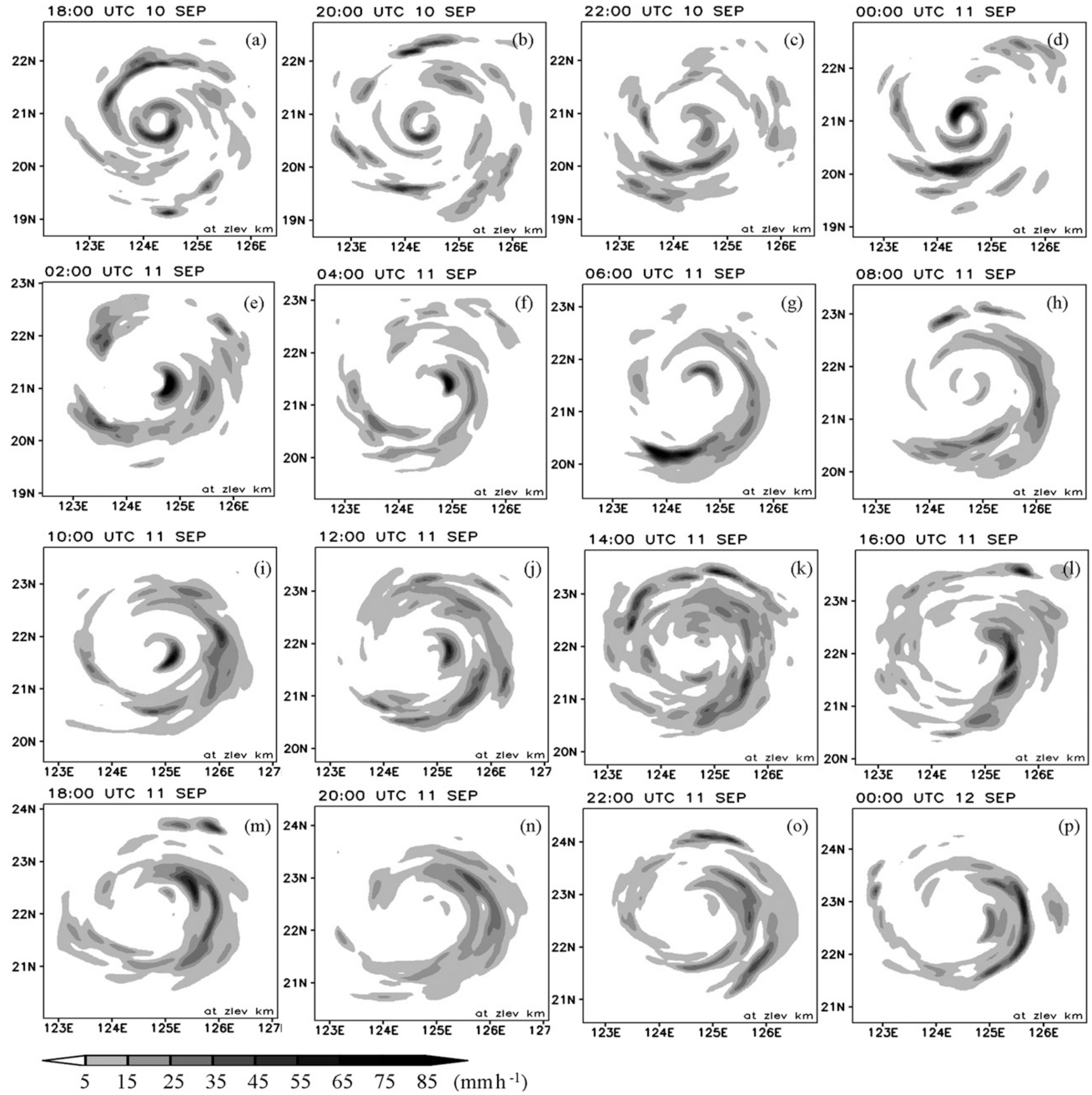

FIG. 9. As in Fig. 7, but for the total column rain rate (mm h$^{-1}$).

than CTL_m and EXP1103_m. Although the secondary eyewall establishes at around the same time in these three different experiments, the duration of CE cycles differs from each other. The eyewall replacement is completed at 1800, 2300, and 1400 UCT 11 September in CTL_m, EXP1103_m, and EXP1015_m, respectively. In other words, the CE cycles of the ensemble means in CTL_m, EXP1103_m, and EXP1015_m last for 11, 16, and 7 h, respectively. The above differences in the duration of CE cycles show the run-to-run variability amid the experiments with different amounts of data assimilated.

As shown in the plan view plots for CTL_m (Figs. 7–11), 5 h after SEF, a transition period (between 1200 and 1800 UTC 11 September) occurs where the CE structure becomes less distinct. During the same period, however, the CE structure in EXP1103 remains evident in terms of either tangential wind or PV, except at 1400 UTC 11 September (Fig. 15). It is not clear why such a transition of eyewall evolution occurs. Further investigation

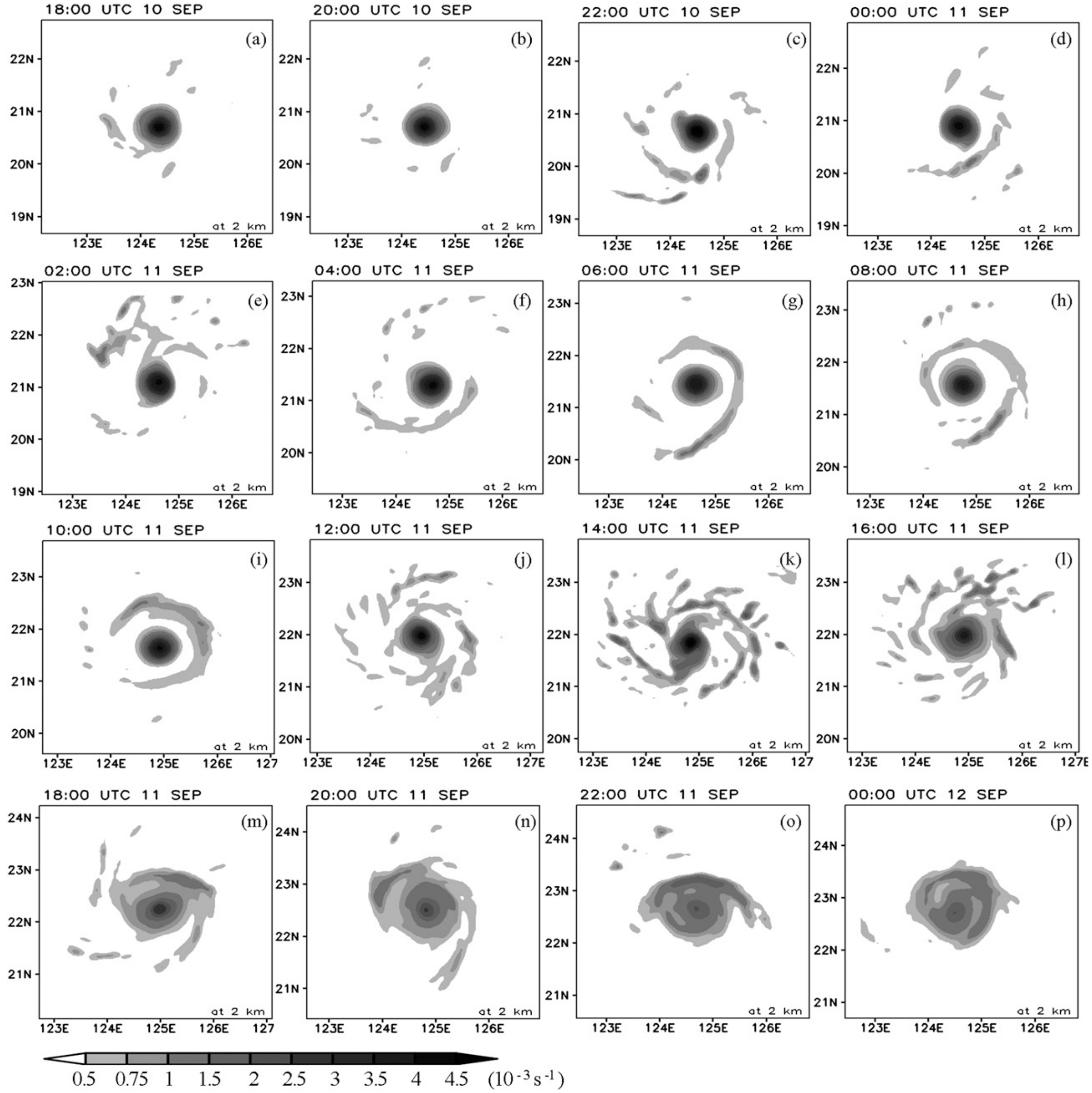

FIG. 10. As in Fig. 7, but for the relative vorticity ($10^{-3}$ s$^{-1}$) at 2-km height.

on possible factors still needs to be carried out, such as the involved PV dynamics (e.g., barotropic instability) and the impact of data assimilation (especially the assimilated azimuthal-mean surface wind).

With the least cumulative data assimilated, the storm track (Fig. 4c), intensity, and structure are not well captured in EXP1003 (Fig. 16). Without assimilating enough updated data, the storm vortex in EXP1003 weakens significantly during early stages of the integration (Fig. 16). The RMTW (Fig. 16a) at 0000 UTC 11 September is about 60 km, approximately 30 km larger than that at the initial time (0300 UCT 10 September). Later, the vortex starts to intensify since 0500 UTC, which is close to the SEF time in other experiments. At the beginning of the intensification, the RMTW of the storm persistently expands, but its intensity does not change significantly (Fig. 16a). Eyewall contraction starts after 1200 UTC 11 September, along with a significant increase in intensity until the end of the integration (Fig. 16a). All the dynamical variables in Fig. 16, such as $\overline{v}$, $\overline{w}$, $\overline{\zeta}$, $\overline{q}$, and the total column rain rate show that there is no coherent CE structure in EXP1003. These results demonstrate that

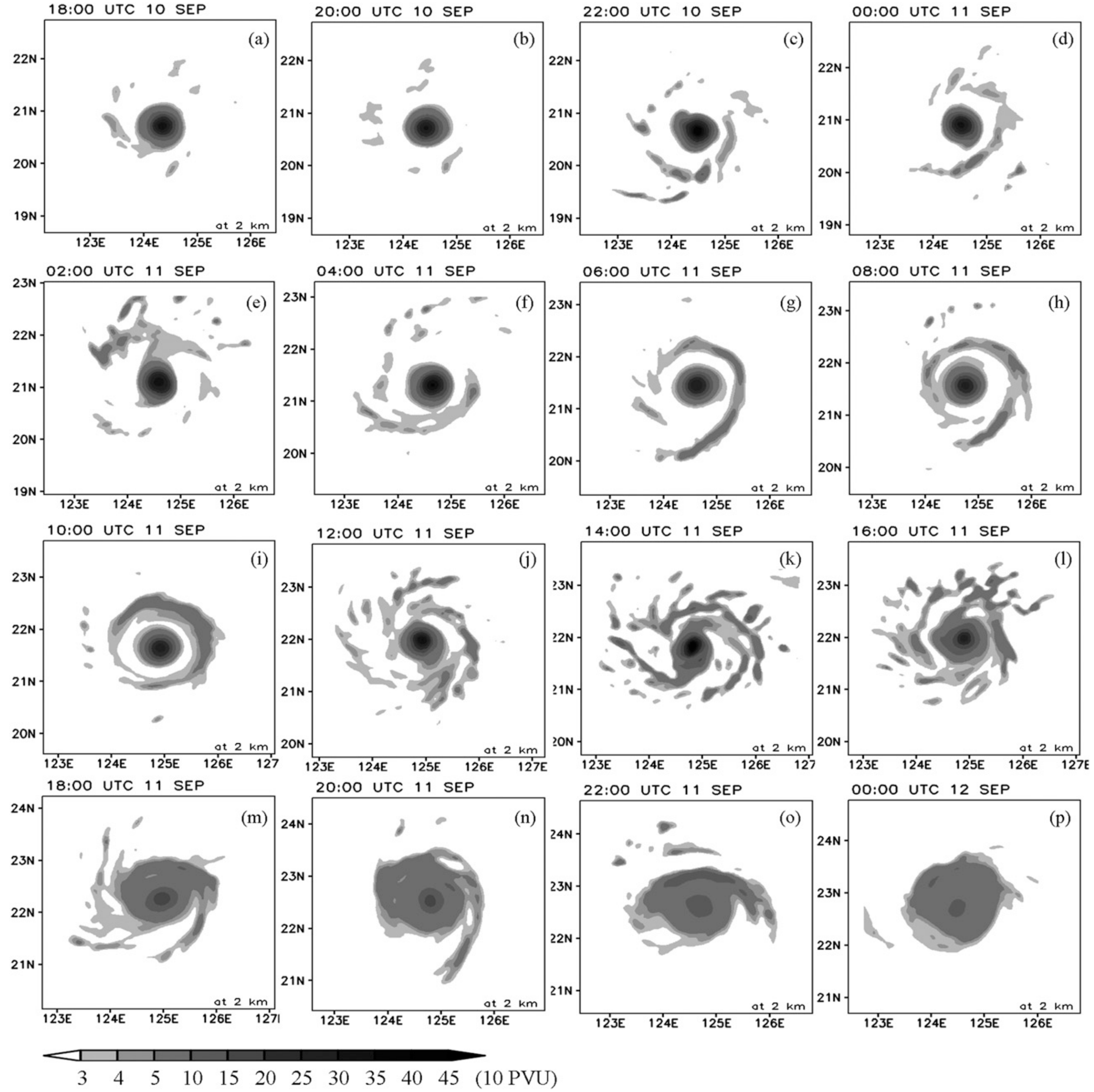

FIG. 11. As in Fig. 7, but for the potential vorticity (10 PVU) at 2-km height.

when less data are assimilated (such as in EXP1003), the storm is weaker (Figs. 4f and 16), and that the simulated tracks have a large northeastward bias as compared to the best track (Fig. 4c), as well as a higher spread among the ensemble members as compared to that in CTL.

## 4. Conclusions

Many possible mechanisms and conditions for SEF have been suggested in the literature. However, insufficient data in a TC vortex and the incomplete understanding on TC dynamics limit our ability to investigate the issue of SEF, leaving the exploration of SEF a challenging issue. Typhoon Sinlaku (2008) is a case in point under T-PARC with the most abundant aircraft observations taken and with great potential to address major scientific issues in T-PARC, such as structure change, targeted observations, and extratropical transition. Meanwhile, an effective TC initialization method featured with three key TC parameters (TC position, motion vector, and the axisymmetric surface wind profile) has been developed in the WRF-based EnKF data assimilation system (Wu et al. 2010). A

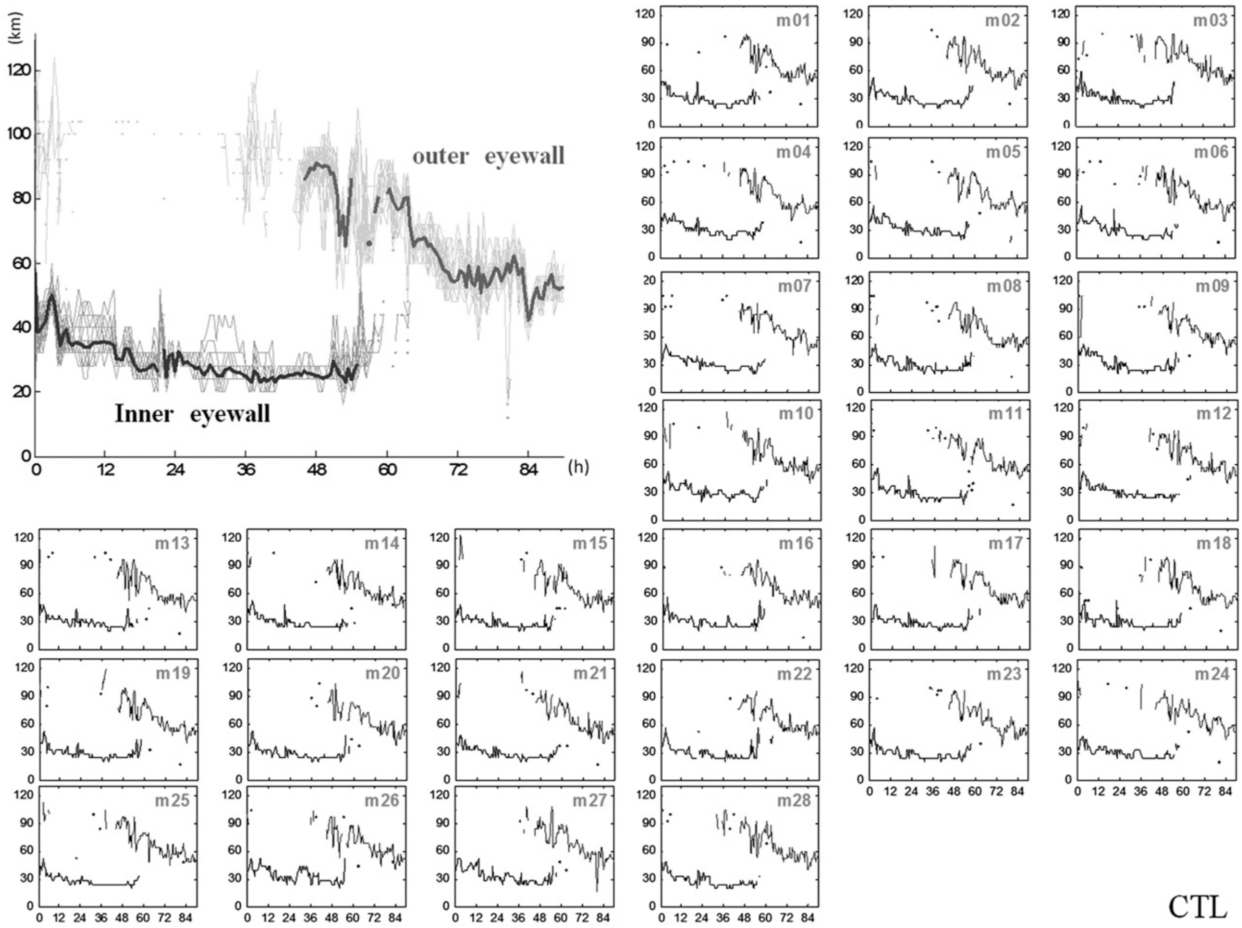

FIG. 12. Evolution of the radii of the (local) maximum tangential wind (km; $y$ axis) for the inner and outer eyewalls based on $\overline{v}$ at the lowest model level. The $x$ axis indicates the integration time (h). The thick line in the main plot demonstrates the ensemble mean, while gray lines indicate the 28 ensemble members, which are also plotted separately in the small figures.

high-temporal/spatial-resolution and model-observation-consistent dataset is thus constructed by continuously assimilating all available conventional soundings, 159 dropwindsondes, and SFMR data from 9 T-PARC flight missions during Sinlaku from 9 to 13 September.

The CE cycle of Sinlaku is demonstrated in CTL in terms of several different parameters ($v$, $u$, $w$, $\zeta$, $q$, and the total column rain rate). Forecast experiments with more data assimilated, such as in EXP1103 and EXP1015, also depict a coherent CE cycle in Sinlaku. It is interesting that the SEF of Sinlaku can be captured in simulations with 5-km horizontal resolution, which is coarser than the critical resolution suggested in previous numerical studies (e.g., Houze et al. 2007). This finding indicates that the assimilation of the valuable extra data into the model along with an appropriate vortex initialization scheme provides special added value to better reconstruct a model/observation-consistent dataset for Sinlaku. This dataset sketches a path to the investigation on Sinlaku's CE formation and evolution. Meanwhile, coherent precursory features of SEF are presented, such as the broadening of the tangential wind, intensification of inflow in the boundary layer, and the weak secondary maximum in azimuthal averages of $\overline{w}$, $\overline{\zeta}$, and $\overline{q}$ projected by sporadic convective activities in spiral rainbands.

Simulations of Sinlaku are performed at different initial times to assess the impact of cumulative data in different amounts. It is striking that some of the simulations are able to capture secondary eyewall cycles (e.g., EXP1103 and EXP1015), while others starting earlier with less data assimilated (e.g., EXP1003) are not. The simulations that are unable to reproduce Sinlaku's CE cycle actually show an overall poor performance on the storm evolution, including its movement and intensity. This result demonstrates that without sufficient data assimilated, numerical simulations of a TC, in particular the structure and intensity change, can be considerably constrained by the model resolution and

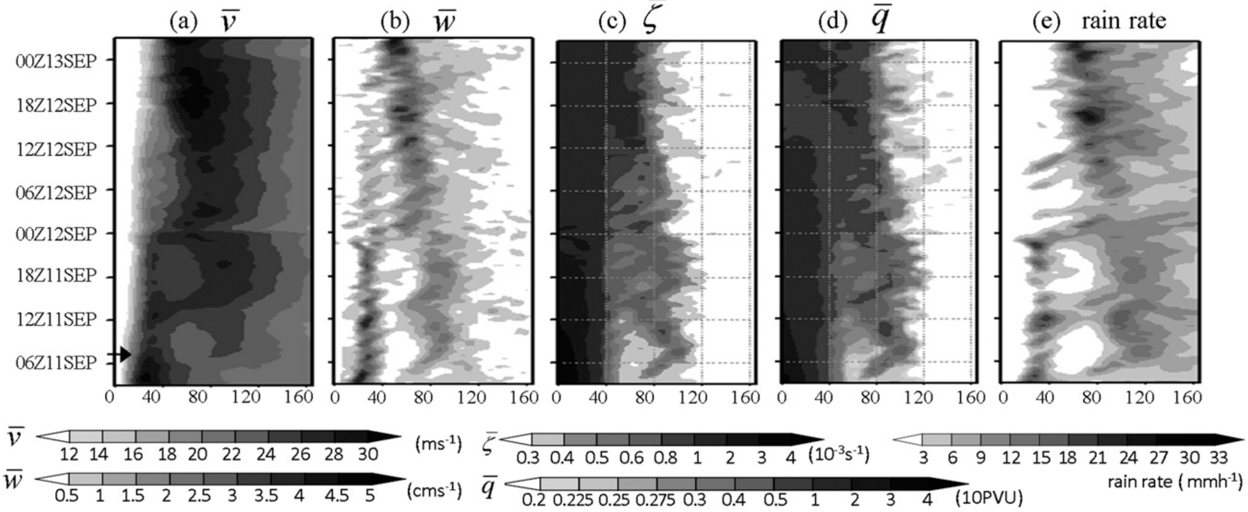

FIG. 13. As in Fig. 5, but for EXP1103_m.

the detailed physical processes in the model setting. On the other hand, results among these simulations also demonstrate the added value of the assimilated data in the framework with 5-km model resolution and a 30-min update cycle. However, quantitative evaluation of impacts of these cumulative data on the vortex and the environmental conditions still requires more sensitivity experiments with suitable numerical design.

We herein stress that although continuous data assimilation significantly affects this dataset of Sinlaku, it is an influence accumulated over a period of time. The applied data assimilation strategy and its corresponding settings do not generate sharp changes at each update cycle (figures not shown). In other words, new data are progressively picked up by the model. The evolution of the continuous model data does not deviate from the model dynamics too much but instead, resembles the results from observation. In addition, concerning the vortex structure, only surface symmetric wind profiles, which are one-dimensional data, are used as a special TC parameter for data assimilation. For this reason, a numerical model must have played a very

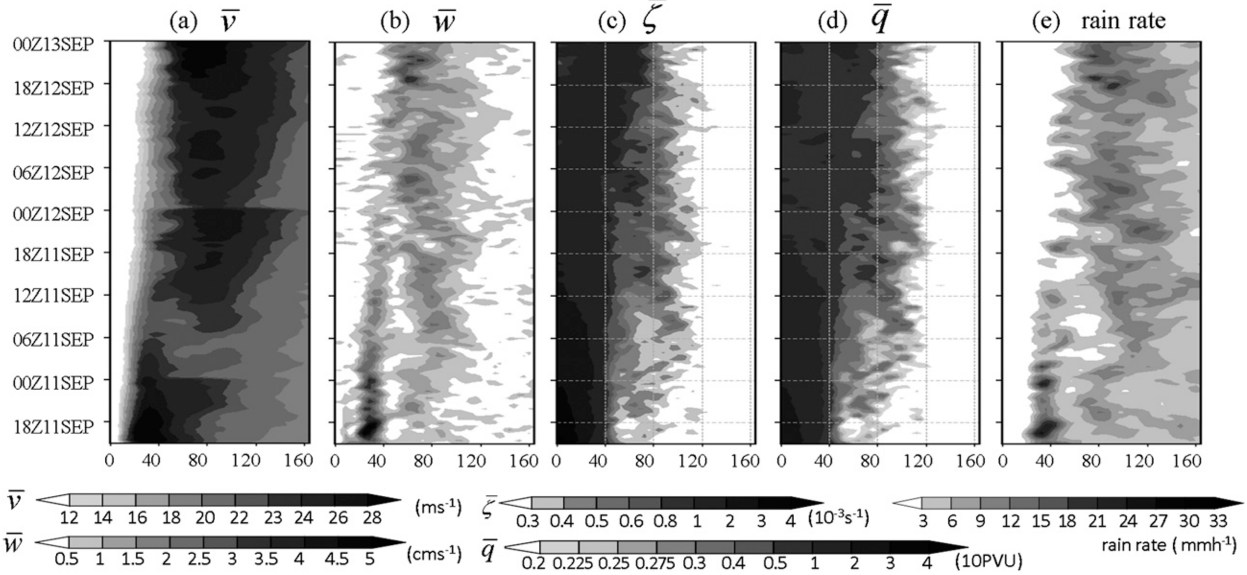

FIG. 14. As in Fig. 13, but for EXP1015_m. Note that the shading interval for (a) is slightly different from that in Fig. 13 to better present the CE structure in EXP1015_m.

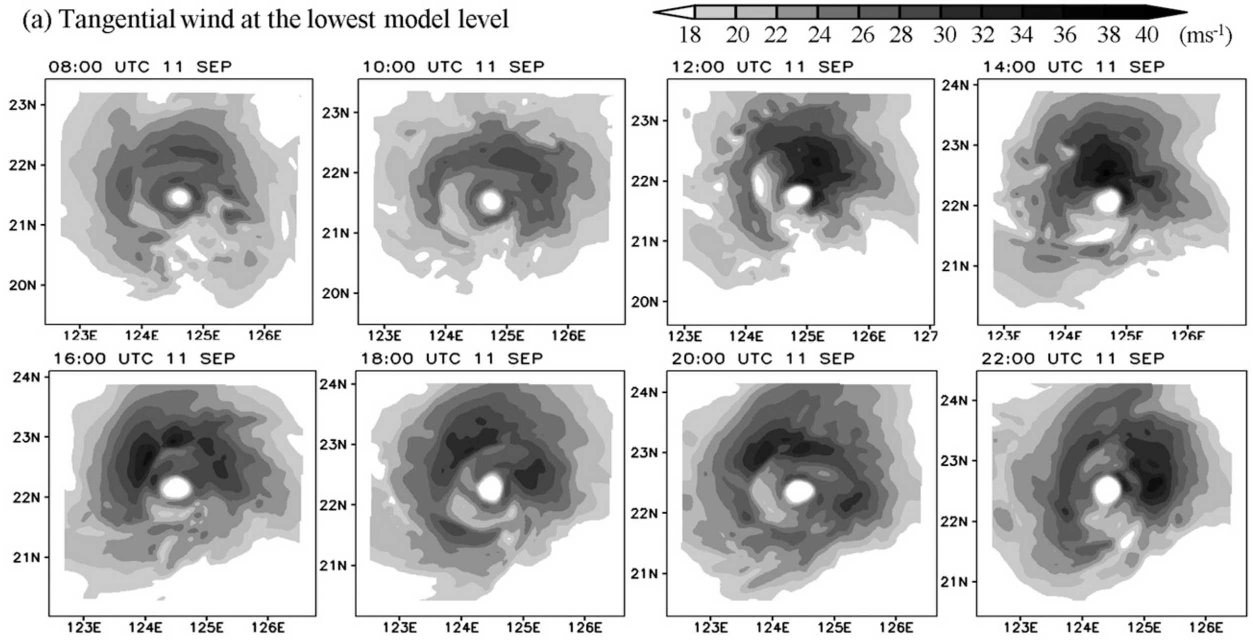
(a) Tangential wind at the lowest model level

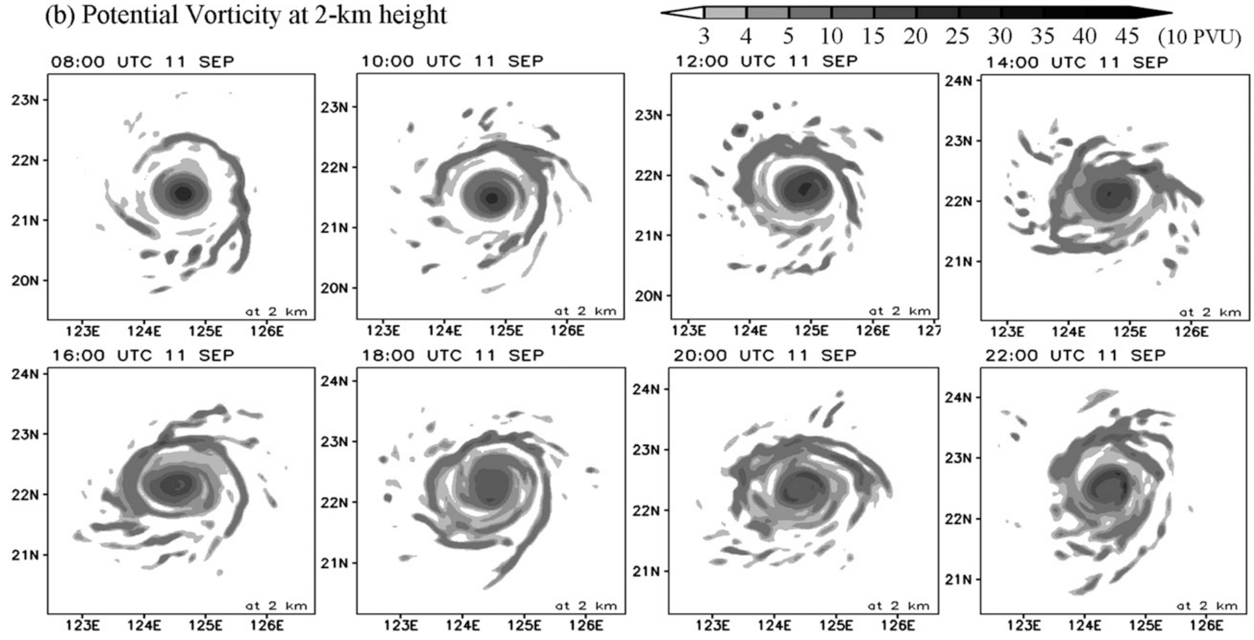
(b) Potential Vorticity at 2-km height

FIG. 15. Plan view of the (a) tangential winds at the lowest model level and (b) potential vorticity at 2-km height in EXP1103_m from 0800 UTC 11 Sep to 2200 UTC 11 Sep with 2-h time intervals.

important role in constructing the three-dimensional vortex evolution, the development of asymmetry features, and the associated wave–mean flow interaction. In short, a good data assimilation method and a capable model work together to compensate the deficiencies of limited observation samplings both temporally and spatially, while good data from observation and an effective data assimilation methodology improve the model output. It is the coordination of observation, the data assimilation method, and the numerical model that generates such a special model/observation-consistent dataset for Sinlaku and constructs an applicable and effective numerical system.

In upcoming papers, we aim to explore the formation of the secondary eyewall with data that can best assess the real atmosphere. In Part II, the precursors to SEF

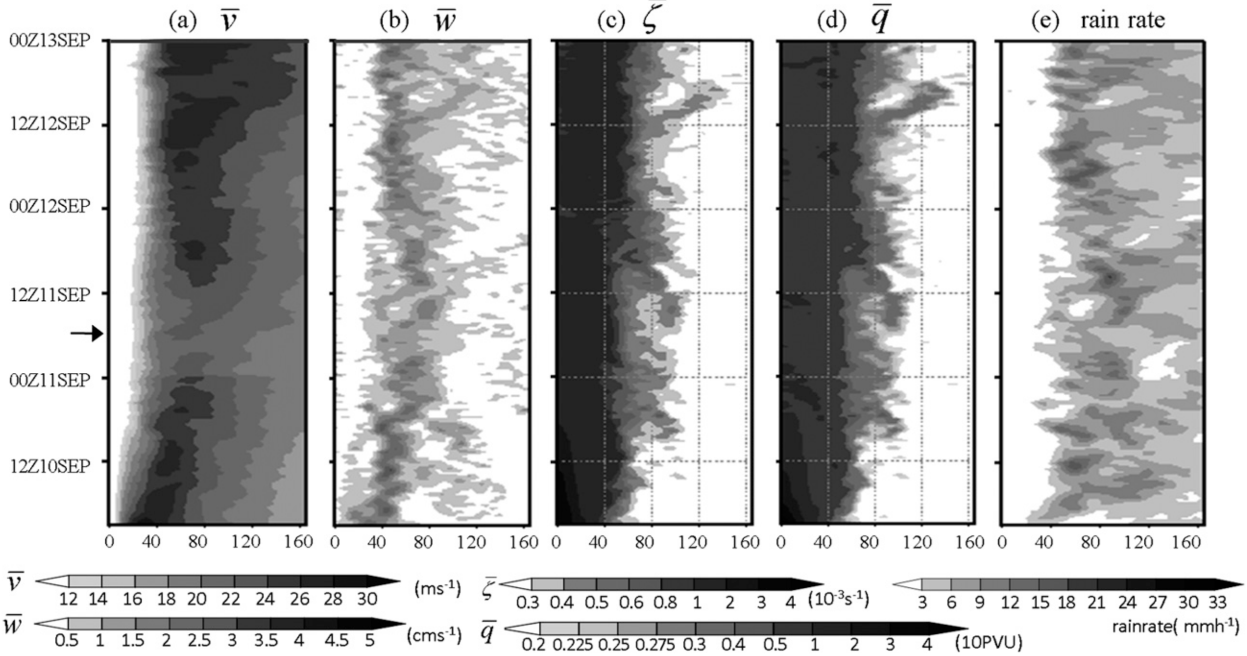

FIG. 16. As in Fig. 13, but for the ensemble mean of EXP1003_m.

are investigated in detail and a new paradigm for SEF in terms of an axisymmetric view is presented. Model output data with a finer time interval (e.g., 2 min) during model simulations and the innovation data during an update cycle of an individual ensemble member are being investigated for further dynamical analyses and will be presented in other upcoming papers. We herein believe that this dataset, which agrees well with the observation, can shed light on our understanding about the formation of the secondary eyewall.

*Acknowledgments.* This work is supported by the National Science Council of Taiwan Grants (NSC 98-2111-M-002-008-MY3 and NSC 97-2111-M-002-016-MY3), Central Weather Bureau Grant (MOTC-CWB-97-6M-01), Office of Naval Research Grant (N00173-08-1-G007), and the Academia Sinica. Team efforts (Pat Harr and Tetsuo Nakazawa) in collecting the data during T-PARC and helpful discussions on EnKF data assimilation with Fuqing Zhang are highly appreciated.

## REFERENCES

Abarca, S. F., and K. L. Corbosiero, 2011: Secondary eyewall formation in WRF simulations of Hurricanes Rita and Katrina (2005). *Geophys. Res. Lett.,* **38,** L07802, doi:10.1029/2011GL047015.

Black, M. L., and H. E. Willoughby, 1992: The concentric eyewall cycle of Hurricane Gilbert. *Mon. Wea. Rev.,* **120,** 947–957.

Brunet, G., and M. T. Montgomery, 2002: Vortex Rossby waves on smooth circular vortices. Part I: Theory. *Dyn. Atmos. Oceans,* **35,** 153–177.

Chen, Y., and M. K. Yau, 2001: Spiral bands in a simulated hurricane. Part I: Vortex Rossby wave verification. *J. Atmos. Sci.,* **58,** 2128–2145.

——, and C. Snyder, 2007: Assimilating vortex position with an ensemble Kalman filter. *Mon. Wea. Rev.,* **135,** 1828–1845.

——, G. Brunet, and M. K. Yau, 2003: Spiral bands in a simulated hurricane. Part II: Wave activity diagnostics. *J. Atmos. Sci.,* **60,** 1239–1256.

Chou, K.-H., C.-C. Wu, P.-H. Lin, S. D. Aberson, M. Weissmann, F. Harnisch, and T. Nakazawa, 2011: The impact of dropwindsonde observations on typhoon track forecasts in DOTSTAR and T-PARC. *Mon. Wea. Rev.,* **139,** 1728–1743.

Corbosiero, K. L., J. Molinari, A. R. Aiyyer, and M. L. Black, 2006: The structure and evolution of Hurricane Elena (1985). Part II: Convective asymmetries and evidence for vortex Rossby waves. *Mon. Wea. Rev.,* **134,** 3073–3091.

Dritschel, D. G., and D. Waugh, 1992: Quantification of the inelastic interaction of unequal vortices in two-dimensional vortex dynamics. *Phys. Fluids,* **4A,** 1737–1744.

Dudhia, J., 1989: Numerical study of convection observed during the Winter Monsoon Experiment using a mesoscale two-dimensional model. *J. Atmos. Sci.,* **46,** 3077–3107.

Elsberry, R. L., and P. A. Harr, 2008: Tropical cyclone structure (TCS08) field experiment science basis, observational platforms, and strategy. *Asia-Pac. J. Atmos. Sci.,* **44** (3), 209–231.

Evensen, G., 1994: Sequential data assimilation with a nonlinear quasi-geostrophic model using Monte Carlo methods to forecast error statistics. *J. Geophys. Res.,* **99,** 10 143–10 162.

Fuentes, O. U. V., 2004: Vortex filamentation its onset and its role on axisymmetrization and merger. *Dyn. Atmos. Oceans,* **40,** 23–42.

Fujita, T., D. J. Stensrud, and D. C. Dowell, 2008: Using precipitation observations in a mesoscale short-range ensemble analysis and forecasting system. *Wea. Forecasting,* **23,** 357–372.

Grell, G. A., and D. Dévényi, 2002: A generalized approach to parameterizing convection combining ensemble and data assimilation techniques. *Geophys. Res. Lett.,* **29,** 1693, doi:10.1029/2002GL015311.

Harnisch, F., and M. Weissmann, 2010: Sensitivity of typhoon forecasts to different subsets of targeted dropsonde observations. *Mon. Wea. Rev.,* **138,** 2664–2680.

Hawkins, H. F., 1983: Hurricane Allen and island obstacles. *J. Atmos. Sci.,* **40,** 1360–1361.

Hawkins, J. D., and M. Helveston, 2008: Tropical cyclone multiple eyewall characteristics. Preprints, *28th Conf. on Hurricanes and Tropical Meteorology,* Orlando, FL, Amer. Meteor. Soc., 14B.1. [Available online at http://ams.confex.com/ams/28Hurricanes/techprogram/paper_138300.htm.]

Hill, K. A., and G. M. Lackmann, 2009: Influence of environmental humidity on tropical cyclone size. *Mon. Wea. Rev.,* **137,** 3294–3315.

Hong, S.-Y., and J.-O. J. Lim, 2006: The WRF single-moment 6-class microphysics scheme (WSM6). *J. Korean Meteor. Soc.,* **42,** 129–151.

——, J. Dudhia, and S.-H. Chen, 2004: A revised approach to ice microphysical processes for the bulk parameterization of clouds and precipitation. *Mon. Wea. Rev.,* **132,** 103–120.

——, Y. Noh, and J. Dudhia, 2006: A new vertical diffusion package with an explicit treatment of entrainment processes. *Mon. Wea. Rev.,* **134,** 2318–2341.

Houze, R. A., and Coauthors, 2006: The Hurricane Rainband and Intensity Change Experiment: Observations and modeling of Hurricanes Katrina, Ophelia, and Rita. *Bull. Amer. Meteor. Soc.,* **87,** 1503–1521.

——, S. S. Chen, B. F. Smull, W.-C. Lee, and M. M. Bell, 2007: Hurricane intensity and eyewall replacement. *Science,* **315,** 1235–1239.

Huang, Y.-H., M. T. Montgomery, and C.-C. Wu, 2012: Concentric eyewall formation in Typhoon Sinlaku (2008). Part II: Axisymmetric dynamical processes. *J. Atmos. Sci.,* **69,** 662–674.

Kossin, J. P., and M. Sitkowski, 2009: An objective model for identifying secondary eyewall formation in hurricanes. *Mon. Wea. Rev.,* **137,** 876–892.

Kuo, H.-C., L.-Y. Lin, C.-P. Chang, and R. T. Williams, 2004: The formation of concentric vorticity structures in typhoons. *J. Atmos. Sci.,* **61,** 2722–2734.

——, C.-P. Chang, Y.-T. Yang, and H.-J. Jiang, 2009: Western North Pacific typhoons with concentric eyewalls. *Mon. Wea. Rev.,* **137,** 3758–3770.

Martinez, Y., G. Brunet, M. K. Yau, and X. Xang, 2011: On the dynamics of concentric eyewall genesis: Space–time empirical normal modes diagnosis. *J. Atmos. Sci.,* **68,** 457–476.

McWilliams, J. C., 1990: The vortices of two-dimensional turbulence. *J. Fluid Mech.,* **219,** 361–385.

Melander, M. V., J. C. McWilliams, and N. J. Zabusky, 1987: Axisymmetrization and vorticity-gradient intensification of an isolated two-dimensional vortex through filamentation. *J. Fluid Mech.,* **178,** 137–159.

Meng, Z., and F. Zhang, 2007: Test of an ensemble Kalman filter for mesoscale and regional-scale data assimilation. Part II: Imperfect model experiments. *Mon. Wea. Rev.,* **135,** 1403–1423.

——, and ——, 2008a: Test of an ensemble Kalman filter for mesoscale and regional-scale data assimilation. Part III: Comparison with 3DVar in a real-data case study. *Mon. Wea. Rev.,* **136,** 522–540.

——, and ——, 2008b: Test of an ensemble Kalman filter for mesoscale and regional-scale data assimilation. Part IV: Comparison with 3DVar in a month-long experiment. *Mon. Wea. Rev.,* **136,** 3671–3682.

Mlawer, E. J., S. J. Taubman, P. D. Brown, M. J. Iacono, and S. A. Clough, 1997: Radiative transfer for inhomogeneous atmospheres: RRTM, a validated correlated-k model for the longwave. *J. Geophys. Res.,* **102** (D14), 16 663–16 682.

Montgomery, M. T., and R. J. Kallenbach, 1997: A theory for vortex Rossby waves and its application to spiral bands and intensity changes in hurricanes. *Quart. J. Roy. Meteor. Soc.,* **123,** 435–465.

——, and G. Brunet, 2002: Vortex Rossby waves on smooth circular vortices. Part II: Idealized numerical experiments for tropical cyclone and polar vortex interiors. *Dyn. Atmos. Oceans,* **35,** 179–204.

Moon, Y., D. S. Nolan, and M. Iskandarani, 2010: On the use of two-dimensional incompressible flow to study secondary eyewall formation in tropical cyclones. *J. Atmos. Sci.,* **67,** 3765–3773.

Nong, S., and K. A. Emanuel, 2003: A numerical study of the genesis of concentric eyewalls in hurricane. *Quart. J. Roy. Meteor. Soc.,* **129,** 3323–3338.

Ortt, D., and S. S. Chen, 2006: Rainbands and secondary eye wall formation as observed in RAINEX. Preprints, *27th Conf. on Hurricanes and Tropical Meteorology,* Monterey, CA, Amer. Meteor. Soc., 12A.5. [Available online at http://ams.confex.com/ams/pdfpapers/108643.pdf.]

——, and ——, 2008: Effect of environmental moisture on rainbands in Hurricane Katrina and Rita (2005). Preprints, *28th Conf. on Hurricanes and Tropical Meteorology,* Orlando, FL, Amer. Meteor. Soc., 5C.5. [Available online at http://ams.confex.com/ams/pdfpapers/138161.pdf.]

Qiu, X., Z.-M. Tan, and Q. Xiao, 2010: The roles of vortex Rossby waves in hurricane secondary eyewall formation. *Mon. Wea. Rev.,* **138,** 2092–2109.

Rozoff, C. M., W. H. Schubert, B. D. McNoldy, and J. P. Kossin, 2006: Rapid filamentation zones in intense tropical cyclones. *J. Atmos. Sci.,* **63,** 325–340.

Samsury, C. E., and E. J. Zipser, 1995: Secondary wind maxima in hurricanes: Airflow and relationship to rainbands. *Mon. Wea. Rev.,* **123,** 3502–3517.

Snyder, C., and F. Zhang, 2003: Assimilation of simulated Doppler radar observations with an ensemble Kalman filter. *Mon. Wea. Rev.,* **131,** 1663–1677.

Terwey, W. D., and M. T. Montgomery, 2008: Secondary eyewall formation in two idealized, full-physics modeled hurricanes. *J. Geophys. Res.,* **113,** D12112, doi:10.1029/2007JD008897.

Torn, R. D., and G. J. Hakim, 2009: Ensemble data assimilation applied to RAINEX observations of Hurricane Katrina (2005). *Mon. Wea. Rev.,* **137,** 2817–2829.

Wang, Y., 2002a: Vortex Rossby waves in a numerically simulated tropical cyclone. Part I: Overall structure, potential vorticity, and kinetic energy budgets. *J. Atmos. Sci.,* **59,** 1213–1238.

——, 2002b: Vortex Rossby waves in a numerically simulated tropical cyclone. Part II: The role in tropical cyclone structure and intensity changes. *J. Atmos. Sci.,* **59,** 1239–1262.

——, 2008: Rapid filamentation zone in a numerically simulated tropical cyclone. *J. Atmos. Sci.,* **65,** 1158–1181.

——, 2009: How do outer spiral rainbands affect tropical cyclone structure and intensity? *J. Atmos. Sci.,* **66,** 1250–1273.

Weissmann, M., and Coauthors, 2011: The influence of assimilating dropsonde data on typhoon track and midlatitude forecasts. *Mon. Wea. Rev.,* **139,** 908–920.

Willoughby, H. E., 1979: Excitation of spiral bands in hurricanes by interaction between the symmetric mean vortex and a shearing environmental steering current. *J. Atmos. Sci.,* **36,** 1226–1235.

——, and P. G. Black, 1996: Hurricane Andrew in Florida: Dynamics of a disaster. *Bull. Amer. Meteor. Soc.,* **77,** 543–549.

——, J. A. Clos, and M. G. Shoreibah, 1982: Concentric eyewalls, secondary wind maxima, and the evolution of the hurricane vortex. *J. Atmos. Sci.,* **39,** 395–411.

——, H.-L. Jin, S. J. Lord, and J. M. Piotrowicz, 1984: Hurricane structure and evolution as simulated by an axisymmetric, nonhydrostatic numerical model. *J. Atmos. Sci.,* **41,** 1169–1186.

——, R. W. R. Darling, and M. E. Rahn, 2006: Parametric representation of the primary hurricane vortex. Part II: A new family of sectionally continuous profiles. *Mon. Wea. Rev.,* **134,** 1102–1120.

Wu, C.-C., K.-H. Chou, H.-J. Cheng, and Y. Wang, 2003: Eyewall contraction, breakdown and reformation in a landfalling typhoon. *Geophys. Res. Lett.,* **30,** 1887, doi:10.1029/2003GL017653.

——, and Coauthors, 2005: Dropwindsonde Observations for Typhoon Surveillance near the Taiwan Region (DOTSTAR): An overview. *Bull. Amer. Meteor. Soc.,* **86,** 787–790.

——, K.-H. Chou, P.-H. Lin, S. D. Aberson, M. S. Peng, and T. Nakazawa, 2007: The impact of dropwindsonde data on typhoon track forecasts in DOTSTAR. *Wea. Forecasting,* **22,** 1157–1176.

——, H.-J. Cheng, Y. Wang, and K.-H. Chou, 2009: A numerical investigation of the eyewall evolution in a landfalling typhoon. *Mon. Wea. Rev.,* **137,** 21–40.

——, G.-Y. Lien, J.-H. Chen, and F. Zhang, 2010: Assimilation of tropical cyclone track and structure based on the ensemble Kalman filter (EnKF). *J. Atmos. Sci.,* **67,** 3806–3822.

Yano, J.-I., and K. A. Emanuel, 1991: An improved model of the equatorial troposphere and its coupling with the stratosphere. *J. Atmos. Sci.,* **48,** 377–389.

Yussouf, N., and D. J. Stensrud, 2010: Impact of phased-array radar observations over a short assimilation period: Observing System Simulation Experiments using an ensemble Kalman. *Mon. Wea. Rev.,* **138,** 517–538.

Zhang, F., and C. Snyder, 2007: Ensemble-based data assimilation. *Bull. Amer. Meteor. Soc.,* **88,** 565–568.

——, ——, and J. Sun, 2004: Impacts of initial estimate and observation availability on convective-scale data assimilation with an ensemble Kalman filter. *Mon. Wea. Rev.,* **132,** 1238–1253.

——, Z. Meng and A. Aksoy, 2006: Test of an ensemble Kalman filter for mesoscale and regional-scale data assimilation. Part I: Perfect model experiments. *Mon. Wea. Rev.,* **134,** 722–736.

——, Y. Weng, J. A. Sippel, Z. Meng, and C. H. Bishop, 2009: Cloud-resolving hurricane initialization and prediction through assimilation of Doppler radar observations with an ensemble Kalman filter: Humberto (2007). *Mon. Wea. Rev.,* **137,** 2105–2125.

Zhou, X., and B. Wang, 2011: Mechanism of concentric eyewall replacement cycles and associated intensity change. *J. Atmos. Sci.,* **68,** 972–988.